

## A numerical tool for modelling oscillating wave surge converter with nonlinear mechanical constraints

M. Brito <sup>a,\*</sup>, R.B. Canelas <sup>a</sup>, O. García-Feal <sup>b</sup>, J.M. Domínguez <sup>b</sup>, A.J.C. Crespo <sup>b</sup>, R.M.L. Ferreira <sup>a</sup>, M.G. Neves <sup>c</sup>, L. Teixeira <sup>d</sup>

<sup>a</sup> CERIS, Instituto Superior Técnico, Universidade de Lisboa, Av. Rovisco Pais, 1049-001, Lisboa, Portugal

<sup>b</sup> EPHYSLAB, Environmental Physics Laboratory, Universidade de Vigo, Campus As Lagoas, 32004, Ourense, Spain

<sup>c</sup> Harbours and Maritime Structures Division, Hydraulics and Environment Department, Laboratório Nacional de Engenharia Civil (LNEC), Av. do Brasil 101, 1700-066, Lisboa, Portugal

<sup>d</sup> Instituto de Mecánica de los Fluidos e Ingeniería Ambiental (IMFIA), Facultad de Ingeniería, Universidad de la República, Uruguay



### ARTICLE INFO

#### Article history:

Received 1 October 2018

Received in revised form

4 August 2019

Accepted 5 August 2019

Available online 7 August 2019

#### Keywords:

Numerical modelling

Smoothed particle hydrodynamics (SPH)

Oscillating wave surge converter (OWSC)

Mechanical constraints

Wave energy

Wave-structure interaction

### ABSTRACT

Mechanical constraints have a non-negligible influence in the motion of oscillating wave surge converter (OWSC) devices. The key novelty of this paper is a numerical simulation tool for OWSCs that does not neglect or significantly compromise mechanical constraints such as hydraulic power take-off (PTO) system, revolute joints and frictional contacts among components. The paper is aimed at presenting the key components of the numerical simulation tool and at validating it with laboratory data featuring an OWSC with mechanical constraints under regular and irregular waves. It is based on the implementation of the multibody solver of Project Chrono under the Smoothed Particle Hydrodynamics (SPH) model of DualSPHysics, where the SPH solver resolves the interaction between wave and flap and the multibody solver resolves the interaction between flap and mechanical constraints. Comparison between numerical results and experimental data show that the numerical simulation tool properly predicts the dynamics of the OWSC. Furthermore, in what concerns hydrodynamics of the near-flap flow, the computed and measured free-surface elevations and phase-averaged flow field show reasonable agreement. Once properly validated, the numerical simulation tool is then applied to study the influence of several mechanical constraints, PTO damping characteristics and flap inertia on the hydrodynamic of the OWSC. The viability of OWSC design solutions based on the developed numerical simulation tool is emphasised, in view of its performance in the test cases to which it was subjected.

© 2019 Elsevier Ltd. All rights reserved.

### 1. Introduction

The first stage of energy conversion of an oscillating wave surge converter (OWSC) device consists on the complex interactions between wave and flap and between flap and mechanical constraints, such as hydraulic power take-off (PTO) system, revolute joints, sliders and frictional contacts among components. These mechanical constraints have a non-negligible influence on the motion of OWSC and consequently on its performance [1]. However, most computational fluid dynamics (CFD) codes model these devices in a simplified way, neglecting the nonlinear mechanical constraints. In the literature, only a few works model OWSCs with mechanical

constraints, including the constraint of the PTO system [2–4]. Nevertheless, these constraints are often simplified with only one mechanical joint as a rotational linear spring and/or a damper [5]. Therefore, robust and efficient CFD numerical simulation tools are still needed to aid the design of OWSCs without significant compromises on the description of its mechanical behavior. Developing such tools is a challenging task due to discrete (singular) nature of some mechanical constraints and due to the difference in geometric and time scales, in some cases orders of magnitude apart. It is thus necessary to employ multiscale methods in order to guarantee the well-posedness of the simulation [6].

This paper addresses this research and engineering need. Its fundamental aim is to present the development, including validation with experimental data, of a novel CFD tool suitable to describe the dynamics of OWSCs with mechanical constraints. The paper shows also the application of the tool to determine the influence of

\* Corresponding author.

E-mail address: [moises.brito@tecnico.ulisboa.pt](mailto:moises.brito@tecnico.ulisboa.pt) (M. Brito).

several mechanical constraints, PTO damping characteristics and flap inertia in order to emphasise its robustness and versatility and thus usefulness to serve as a design tool.

Mesh-based methods were considered less appropriate to develop such simulation tool. They have been widely applied in the modelling of OWSCs, e.g., Ansys Fluent [7–9] and OpenFOAM [4,10,11], but they pose difficulties when trying to incorporate mechanical constraints. Firstly, mesh-based methods require computationally expensive and formally complex mesh moving algorithms [6,12], due to the large motion of the flap. Secondly, solving the mechanical constraints usually requires additional mathematical transformations to solve nonlinear complementarity problem, singularities, non-uniqueness, non-penetration, inequality constraint and NP-hardness. These can be more expensive than solving the hydrodynamic interaction between wave and flap [6]. Thirdly, some mechanical constraints (e.g., frictional revolute, prismatic and slider joints) are not, in general, continuous and straightforward application of mesh-based methods for ordinary differential equations (ODEs) require mesh sizes and time steps that can be impracticable [13–15]. Additionally, mesh-based methods need to solve an additional equation, such as Volume-of-Fluid (VOF) method to describe the free-surface.

The hydrodynamic approach of the simulation tool herein developed was the mesh-free method Smooth Particle Hydrodynamics (SPH), widely adopted in the study of complex free-surface flows for its merits to easily calculate interactions between flow and driven bodies [16–19] and more recently to modelling OWSCs [12,20–23]. The free-surface is captured in the SPH method without the need for solving additional equations to describe the free-surface. Moreover, SPH is considered a versatile method, naturally dealing with unsteady and nonlinear flows, extreme deformations and complex topological evolutions, such as a breaking free-surface [24,25]. However, solid boundary conditions do not appear in a natural way in the SPH formalism [16]. Different types of boundary conditions, based on ghost, repulsive and dynamic particles [16], can be implemented in SPH to create a repulsive force that prevents fluid particles from penetrating the limits of the domain or solid boundaries. In this paper, the Dynamic Boundary Condition (DBC) is used [26]. This DBC allows to handle complex geometries in 2D and 3D, and it is easy to implement due to its computational simplicity where the fluid-boundary interactions can be calculated inside the same loops as fluid particles. This boundary condition does not include a specific value to define wall friction. Nevertheless, it is shown below that increasing the resolution improves the solution near the solid walls.

Given the dynamic nature of the SPH formulation, some mechanical constraints are also difficult to include in SPH form, for example lubricated contacts or asperities between driven bodies. Recently [27], have successfully developed a method to overcome the limitations of traditions SPH by coupling a general-purpose Differential Variational Inequality (DVI) based non-smooth multi-body dynamics solver.

The modelling effort builds on these advances. This paper provides a novel CFD tool for modelling OWSCs with mechanical constraints. Structurally, this tool consists on a numerical implementation of the multibody solver of Project Chrono [28] under SPH model of DualSPHysics [29]. The DualSPHysics code is used to solve wave-flap interaction and Project Chrono library is used to solve flap-mechanical constraints interaction. The conceptual and numerical models used for the fluid and multibody description, and numerical implementation of Project Chrono library under DualSPHysics, are presented in Section 2. The tool is validated with measured and reference experimental solutions in Section 3. Section 4 shows the numerical analysis of the OWSC for several mechanical constraints, PTO damping coefficients and flap inertia. The

main conclusions are summarized in Section 5.

## 2. Numerical model

In this section the principal characteristics of the DualSPHysics and Project Chrono are first introduced, focusing on the aspects that are relevant for the simulation of OWSC devices. The coupling procedure is then presented.

### 2.1. DualSPHysics

DualSPHysics is an open-source code base on SPH method [29]. This code is implemented in C++ and Compute Unified Device Architecture (CUDA), allowing to run simulations either on multiple Central Processing Units (CPU) using Open Multi-Processing (OpenMP) or on a Graphics Processing Units (GPU) [30].

In SPH, the fluid is described as a set of discrete particles. Any physical property can be computed as an interpolation of the values of the nearest neighboring particles. The contribution of the neighboring particles is weighted according to their distance from a target particle using a kernel function,  $W$ , and a smoothing length,  $h$  [31,32].

#### 2.1.1. Governing equations

The  $\delta$ -SPH approach [33,34] is followed in this paper. The continuity and Navier-Stokes equations are written as:

$$\frac{d\rho_i}{dt} = \sum_j m_j (\mathbf{v}_i - \mathbf{v}_j) \cdot \nabla_i W(\mathbf{r}_i - \mathbf{r}_j, h) + 2\delta_\phi h c_0 \sum_j (\rho_j - \rho_i) \frac{(\mathbf{r}_i - \mathbf{r}_j) \cdot \nabla_i W(\mathbf{r}_i - \mathbf{r}_j, h)}{(\mathbf{r}_i - \mathbf{r}_j)^2} \frac{m_j}{\rho_j} \quad (1)$$

$$\frac{d\mathbf{v}_i}{dt} = - \sum_j m_j \left( \frac{P_i}{\rho_i^2} + \frac{P_j}{\rho_j^2} + \Pi_{ij} \right) \nabla_i W(\mathbf{r}_i - \mathbf{r}_j, h) + \mathbf{g} \quad (2)$$

where the subscripts  $i$  and  $j$  denote respectively the target and the neighboring particles within the support of the kernel  $W$ ,  $t$  is the time,  $m$  is the mass,  $\rho$  is the density of the fluid,  $c_0$  is the reference speed of sound,  $\mathbf{v}$  is the velocity vector,  $\mathbf{r}$  is the position vector,  $P$  is the pressure,  $\mathbf{g}$  is the gravitational acceleration vector and  $\delta_\phi$  is the  $\delta$ -SPH coefficient that control the intensity of the diffusive term in Equation (1) and  $\Pi$  is the viscous term.

The performance of the SPH method depends heavily on the selection of the kernel  $W$ . The accuracy of the SPH interpolation increases with the order of the polynomials used to define  $W$ . In this paper, a Quintic Wendland kernel suggested by Ref. [35] was used:

$$W(\mathbf{r}_i - \mathbf{r}_j, h) = \alpha_D \begin{cases} \left(1 - \frac{|\mathbf{r}_i - \mathbf{r}_j|}{2h}\right)^4 \left(\frac{2|\mathbf{r}_i - \mathbf{r}_j|}{h} + 1\right) & \text{if } \frac{|\mathbf{r}_i - \mathbf{r}_j|}{h} \leq 2 \\ 0 & \text{if } \frac{|\mathbf{r}_i - \mathbf{r}_j|}{h} > 2 \end{cases} \quad (3)$$

where the coefficient  $\alpha_D = 7/(4\pi h^2)$  for 2D and  $\alpha_D = 21/(16\pi h^3)$  for 3D modelling.

In DualSPHysics the fluid is treated as Weakly Compressible SPH (WCSPH) and the following equation of state is used to determine fluid pressure based on particle density [24,36]:

$$P_i = \frac{c_0^2 \rho_0}{\gamma} \left[ \left( \frac{\rho_i}{\rho_0} \right)^\gamma - 1 \right] \quad (4)$$

where  $\gamma = 7$  is the polytropic constant,  $\rho_0 = 1000 \text{ kg/m}^3$  is the reference density and  $c_0 = c(\rho_0) = \sqrt{\partial P / \partial \rho}|_{\rho_0}$  is the speed of sound at  $\rho_0$  [29].

The viscous term features the artificial viscosity approach proposed by Ref. [33]:

$$\Pi_{ij} = \begin{cases} \frac{-\alpha(c_i + c_j)}{(\rho_i + \rho_j)} \frac{h(\mathbf{v}_i - \mathbf{v}_j)(\mathbf{r}_i - \mathbf{r}_j)}{[(\mathbf{r}_i - \mathbf{r}_j)^2 + 0.01h^2]} & \text{if } (\mathbf{v}_i - \mathbf{v}_j)(\mathbf{r}_i - \mathbf{r}_j) < 0 \\ 0 & \text{if } (\mathbf{v}_i - \mathbf{v}_j)(\mathbf{r}_i - \mathbf{r}_j) \geq 0 \end{cases} \quad (5)$$

where  $\alpha \in [0.01, 0.1]$  is an empirical coefficient.

The simulations were carried out for  $\alpha = 0.01$ . This value was widely used to model both wave propagation and wave impact on structure, since it is the minimum value that prevents instability and spurious oscillations in the numerical scheme [37]. The coefficient  $\delta_\phi = 0.1$  was used. This value is recommended for most applications with open and moving solid boundaries, where a noncomplete kernel is inevitably present, in order to reduce numerical diffusion [29]. In strongly dynamic cases this value contributes with a force that may be several orders of magnitude smaller than the pressure and viscous terms, and does not incur in any type of degradation of the solution.

### 2.1.2. Interaction between fluid and rigid bodies

In SPH, rigid bodies are also described as sets of discrete particles whose variables are integrated in time with a different set of equations [38]. The net force on each boundary particle is the sum of the contributions of all surrounding fluid particles i.e., each body particle experiences a force per unit mass given by:

$$\mathbf{f}_k = \sum_{i \in \mathcal{A}_i} \mathbf{f}_{ki} \quad (6)$$

where  $\mathcal{A}_i$  stands for the fluid particles domain,  $\mathbf{f}_{ki}$  is the force vector per unit mass exerted by the fluid particle  $i$  on the boundary particle  $k$ , which is given by:

$$m_k \mathbf{f}_k = -m_i \mathbf{f}_{ki} \quad (7)$$

For the motion of the moving body, the basic equations of rigid body dynamics can then be used:

$$M \frac{d\mathbf{V}}{dt} = \sum_{k \in \mathcal{A}_k} -m_k \mathbf{f}_k \quad (8)$$

$$\mathbf{I} \frac{d\Omega}{dt} = \sum_{k \in \mathcal{A}_k} -m_k (\mathbf{r}_k - \mathbf{R}_0) \times \mathbf{f}_k \quad (9)$$

where  $\mathcal{A}_k$  stands for the boundary particles domain,  $M$  and  $\mathbf{I}$  are respectively the mass and inertial tensor of the body,  $\mathbf{V}$  is the linear velocity vector of the centre of mass,  $\Omega$  is the angular velocity,  $\mathbf{r}_k$  is the position vector of particle  $k$  and  $\mathbf{R}_0$  is the position vector of the centre of mass. Equations (8) and (9) are integrated in time in order to predict the values of  $\mathbf{V}$  and  $\Omega$  at the beginning of the next time step. Each particle within the body has a velocity given by:

$$\mathbf{v}_k = \mathbf{V} + \boldsymbol{\Omega} \times (\mathbf{r}_k - \mathbf{R}_0) \quad (10)$$

Finally, the particles within the rigid body are moved by integrating Equation (10) in time. In this paper, the time-stepping scheme used is Symplectic [39], namely explicit second-order Symplectic scheme which involves a predictor-corrector strategy. This scheme can preserve geometric features, such as the energy time-reversal symmetry present in the equations of motion, leading to an improved resolution of the long-term solution behavior. A variable time step proposed by Ref. [40] is considered. This is based on the force per unit mass, viscous diffusion term and Courant-Friedrich-Levy (CFL) condition.

[36,41] have demonstrated that Equation (10) allows the conservation of both linear and angular momentum [42], presented successful validations of nonlinear wave interaction with driven bodies in SPH comparing with experimental data that includes deformations in the free-surface due to the presence of driven boxes and the movement of those bodies during the experiment (heave, surge and roll displacements). Several validations using DualSPHysics are performed in Ref. [38] who analyzed the buoyancy-driven motion with solid bodies larger than the smallest flow scales and with various densities.

### 2.1.3. Boundary conditions

The Dynamic Boundary Condition (DBC) is the default method provided by DualSPHysics [26,29]. In this method rigid boundaries (e.g., fixed and moving structures, walls, gates and wavemakers) are described by a set of boundary particles that satisfy the same equations as the fluid particles (i.e., Equations (1), (2) and (4)). These boundary particles have the same properties as the fluid particles, but they do not move in accordance to the forces exerted on them. They remain either in a fixed position (e.g., fixed boundaries) or move according to an imposed/assigned motion function (i.e., moving bodies). An interesting advantage of DBC is its computational simplicity, since boundary particles can be calculated inside the same loops as the fluid ones with a considerable saving of computational time. This DBC has been properly validated in Refs. [43,44].

### 2.2. Multibody dynamics solver

In this paper, the multibody solver used is Project Chrono [28], since its library allows for the simulation of multibody entities with a large number of mechanical constraints, such as joints and sliders, friction and restitution coefficients, restitution forces, and user-imposed forces and trajectories with arbitrary degrees of freedom.

#### 2.2.1. Project Chrono

In Project Chrono, the configuration of a rigid multibody system is described by using six independent coordinates, called generalized coordinates  $\mathbf{q}$ , being  $\mathbf{q} = [\mathbf{R}^\top + \boldsymbol{\Theta}^\top]^\top$ , where  $\mathbf{R}$  and  $\boldsymbol{\Theta}$  are respectively the translational and rotational coordinates, that completely define the location and orientation of each body in the system [13]. Once this set of coordinates is identified, the global position of an arbitrary point on the body can be expressed in terms of  $\mathbf{q}$ . The dynamic of rigid bodies can be characterized by a system of two differential algebraic equations in the following form [15]:

$$\frac{d\mathbf{q}}{dt} = \mathbf{L}(\mathbf{q})\mathbf{V} \quad (11)$$

$$\mathbf{M}(\mathbf{q}) \frac{d\mathbf{V}}{dt} = \mathbf{F}_a(\mathbf{V}, \mathbf{q}, t) + \sum_{i \in \mathcal{A}(\mathbf{q}, \delta)} (\gamma_{i,n} \mathbf{D}_{i,n} + \gamma_{i,u} \mathbf{D}_{i,u} + \gamma_{i,w} \mathbf{D}_{i,w}) \quad (12)$$

where  $\mathbf{L}$  is the Jacobian matrix that connects  $\mathbf{V}$  to the derivative of  $\mathbf{q}$ ,  $\mathbf{M}$  is the inertia matrix,  $\mathbf{F}_a$  is the applied forces,  $\gamma_{i,n}$ ,  $\gamma_{i,u}$  and  $\gamma_{i,w}$  are the Lagrange multiplier and  $\mathbf{D}_{i,n}$ ,  $\mathbf{D}_{i,u}$ , and  $\mathbf{D}_{i,w}$  are the tangent space generators, the subscripts  $n$ ,  $u$  and  $w$  stand for the orientation of local reference frames at contact point  $i$ , where  $n$  is the normal component pointing toward to the exterior of the body, and  $u$  and  $w$  are the tangential components [45]. Equation (11) relates the time derivative of  $\mathbf{q}$  and  $\mathbf{V}$  through a linear transformation defined by  $\mathbf{L}$  while Equation (12) is the force balance that ties the inertial forces to the applied and constraint forces.

The constraint forces are imposed by bilateral restrictions that limit the relative motion of the rigid bodies present in the system. The inclusion states that the frictional contact force lies somewhere inside the friction cone, with a value yet to be determined and controlled by the stick/slip state of the interaction between body and ground [15]. In multibody dynamics, the differential inclusion can be posed as a differential variational inequality problem [46]. Specifically, the unilateral constraints define a set of contact complementarity conditions  $0 \leq \Phi_i(\mathbf{q}) \perp \gamma_{i,n} \geq 0$  which make a simple point: for a potential contact  $i$  in the active set:

$$i \in \mathcal{A}_q(\mathbf{q}, \delta) : \begin{cases} 0 \leq \Phi_i(\mathbf{q}) \perp \gamma_{i,n} \geq 0 \\ (\gamma_{i,u}, \gamma_{i,w}) = \underset{\sqrt{\gamma_{i,u}^2 + \gamma_{i,w}^2} \leq \mu_i \gamma_{i,n}}{\operatorname{argmin}} \mathbf{V}^T \cdot (\gamma_{i,u} \mathbf{D}_{i,u} + \gamma_{i,w} \mathbf{D}_{i,w}) \end{cases} \quad (13)$$

where  $\Phi_i$  is the gap (distance) between two geometries.

For computational efficiency, only the contacts that are imminently active are included in the dynamical resolution and linearized. Their set is denoted by  $i \in \mathcal{A}_q(\mathbf{q}, \delta)$  in Equation (13). The condition  $\Phi_i(\mathbf{q}) \geq 0$  stands for the non-interpenetration constraint

and  $\gamma_{i,n} \geq 0$  stands for the compressive normal impulse exerted at a contact  $i$ . The last condition poses an optimization problem, whose first-order Karush-Kuhn-Tucker optimality conditions are equivalent to the Coulomb dry friction model. The frictional contact force associated with contact  $i$  leads to a set of generalized forces, which are obtained using the projectors  $\mathbf{D}_{i,n}$ ,  $\mathbf{D}_{i,u}$  and  $\mathbf{D}_{i,w}$  [15].

The time stepping used in Project Chrono is a variant of the well-known implicit Euler method for ODEs [45–48].

### 2.3. Coupling procedure

The simulation of wave-OWSC interaction with mechanical constraints using the developed numerical simulation tool is mainly split in three steps. In the first step, DualSPHysics computes the particles interaction by solving the governing equations in SPH form (Equation (1) and (2)). Then the motion of the flap is calculated using the Newton's equations for rigid body dynamics (Equation (8) and (9)). In the second step, the linear,  $d\mathbf{V}/dt$ , and angular acceleration vector,  $d\Omega/dt$ , to be applied in the centre of mass of the flap are transferred to the Project Chrono library. During that time step, Project Chrono updates the motion of the flap, considering the given mechanical constraints and using the multibody dynamic model (Equation (11) and (12)). The value of  $\mathbf{R}_0$ ,  $\mathbf{V}$  and  $\Omega$  are transferred back to the DualSPHysics. In the third step, DualSPHysics updates the position of the particles that form the flap by Equation (10) with the information transferred from Project Chrono library. Finally, DualSPHysics updates the  $\mathbf{r}$ ,  $\mathbf{v}$ ,  $\rho$  and  $P$  of all fluid and boundary particles of the system at the new time step. The flow chart of the solving procedure is presented in Fig. 1.

### 3. Validation of numerical simulation tool

The validation of the numerical simulation tool is mainly performed in three stages. In the first stage, the dynamic behavior of an OWSC with mechanical constraints is validated by comparing measured and computed PTO force given by a given angular velocity of the flap. In the second stage, removing the OWSC model from the wave flume, the wave generation and propagation are

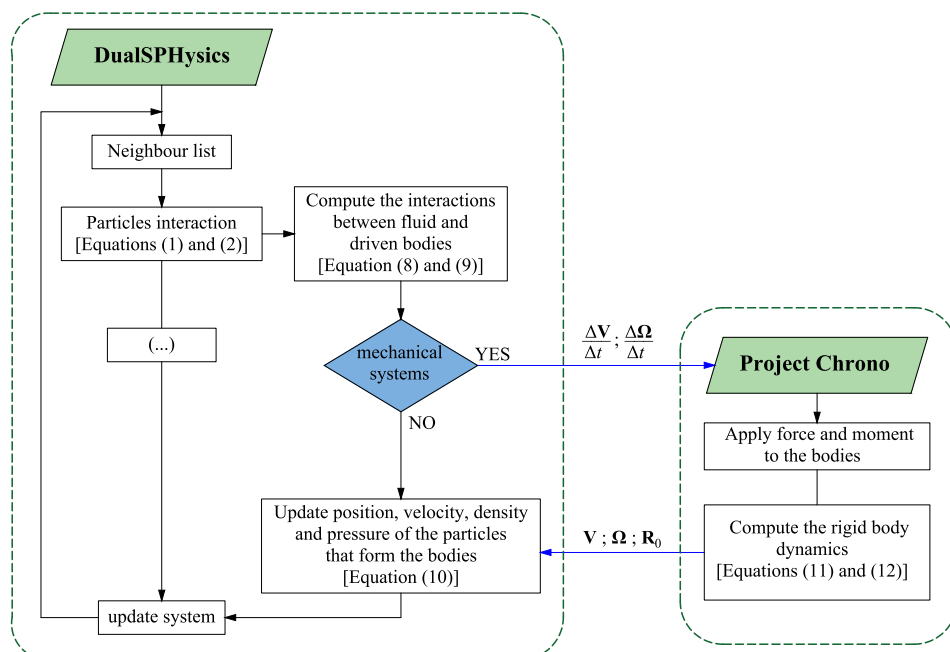


**Fig. 1.** Flow chart of coupling procedure to model wave-OWSC interaction with any mechanical constraints.

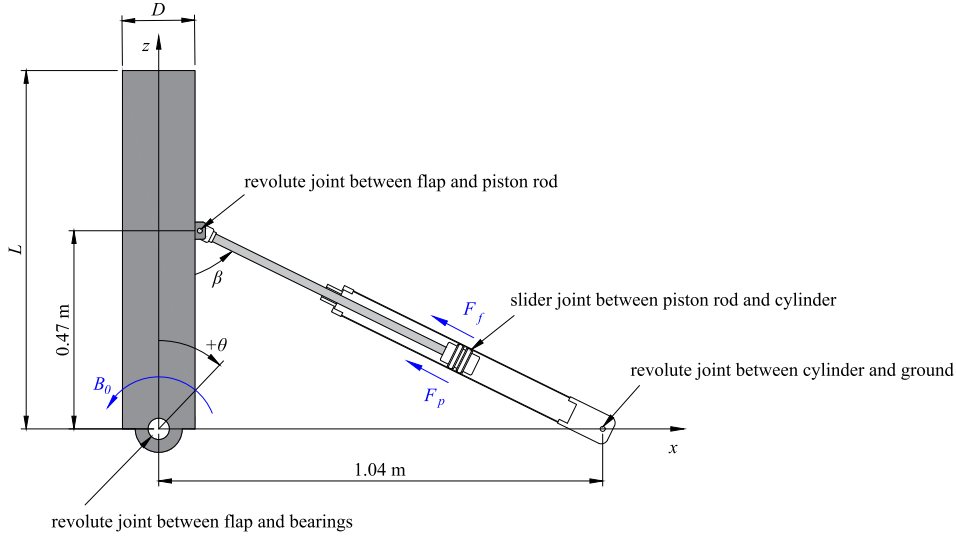


**Fig. 2.** Sketch of the OWSC model implemented in Project Chrono, including the mechanical joints among components.

validated by comparing the free-surface elevation for both regular and irregular waves. In the third stage, the ability to describe flow hydrodynamics resulting from the interaction with the OWSC and ability to describe OWSC dynamics with mechanical constraints are validated by numerical solutions and experimental data of the flap motion and of the flow field.

### 3.1. Dynamics of the OWSC with mechanical constraints

The experimental test presented in Ref. [49] is used here for the validation of the numerical simulation tool. In this test, a 1:10 scale model of an OWSC, composed by a buoyant flap and by a hydraulic PTO system, was driven by an excitation force in order to show the general capabilities of the Project Chrono to predict the dynamic behavior of OWSC under both regular and irregular motion. The side view of the OWSC model implemented in Project Chrono with the mechanical joints among components are shown in Fig. 2.

The flap is attached to the foundation via bearings with internal diameter of 0.05 m, hinged on its horizontal axis. A cartesian coordinate system is used in which  $x$ ,  $y$  and  $z$  refer to the longitudinal, lateral and vertical directions, respectively. The system origin is defined as:  $x = 0$  and  $z = 0$  at the pivot point of the flap;  $y = 0$  at centre plane of the flap. The main characteristics of the flap are given in Table 1.

The PTO system is composed by a hydraulic cylinder, linked to the flap at  $z = 0.47$  m and  $x = 0.09$  m and to the flume bed at  $z = 0$  and  $x = 1.04$  m (see Fig. 2). The constraint force of the PTO system,  $F_{PTO}$ , on the slider joint between piston rod and cylinder is given by:

$$F_{PTO} = F_p + F_f \quad (14)$$

where  $F_p$  and  $F_f$  are respectively the friction and pressure forces of

the hydraulic cylinder (details in Appendix A and Appendix B, respectively). The friction torque on the revolute joint between flap and bearings,  $B_0$  (see Fig. 2), was modelled using the Coulomb friction, with static friction coefficient of 0.16 [49]. An experimental assessment revealed that friction components of the revolute joints between flap and piston rod, and between cylinder and ground were small compared with friction of the revolute joint between flap and bearings as they were systematically within the error margin of the instrumentation. The experimental uncertainty for these measurements is high. For this reason, they were neglected. All parameters and constants here introduced are deeply described in Ref. [49].

The angular velocity of the flap,  $\dot{\theta}$ , during the physical model test (imposed in Project Chrono) and the comparison of the numerical and experimental results of  $F_{PTO}$  are shown in Fig. 3.

In this paper, the agreement between numerical and experimental results is quantified considering two statistical parameters: normalised amplitude error,  $A_\chi$ , and normalised phase-amplitude error,  $\varphi_\chi$ , given respectively by:

$$A_\chi = \sqrt{\frac{\sum_{i=1}^N (\chi_i^{num})^2}{\sum_{i=1}^N (\chi_i^{exp})^2}}; \quad \varphi_\chi = \sqrt{\frac{\sum_{i=1}^N (\chi_i^{num} - \chi_i^{exp})^2}{\sum_{i=1}^N (\chi_i^{exp})^2}} \quad (15)$$

where  $\chi_i$  is the magnitude of the signal to be analyzed,  $N$  is the number of samples, superscripts *num* and *exp* refer to numerical and experimental values, respectively. A perfect agreement between signals would result in  $A_\chi \rightarrow 1$  and  $\varphi_\chi \rightarrow 0$ . The agreement of the time series shown in Fig. 3b is characterized by  $A_\chi = 1.05$  and  $\varphi_\chi = 0.15$ . Note that values of  $A_\chi > 1$  means that the numerical results have overestimated the experimental data in amplitude, however here it is close to 1, which means a good agreement.

Some discrepancies are observed, mostly caused by the asymmetrical characteristic of the experimental hydraulic circuit. In fact, the inclusion of all the dynamic effects in a single model is not an easy task, and it is especially difficult to define a mechanism governing the switch among the check-valves [49]. On the other hand,

**Table 1**

Dimension, mass and moment of inertia (about the bearings) of the flap.

Dimensions	Symbol	Value
Height	$L$	0.84 m
Width	$B$	1.31 m
Thickness	$D$	0.17 m
Mass	$m$	72.3 kg
Moment of inertia	$(I_{xx}; I_{yy}; I_{zz})$	$(27.61; 14.76; 13.11) \text{ kg m}^2$
Centre of mass	$(\bar{x}; \bar{y}; \bar{z})$	$(0; 0; 0.33) \text{ m}$

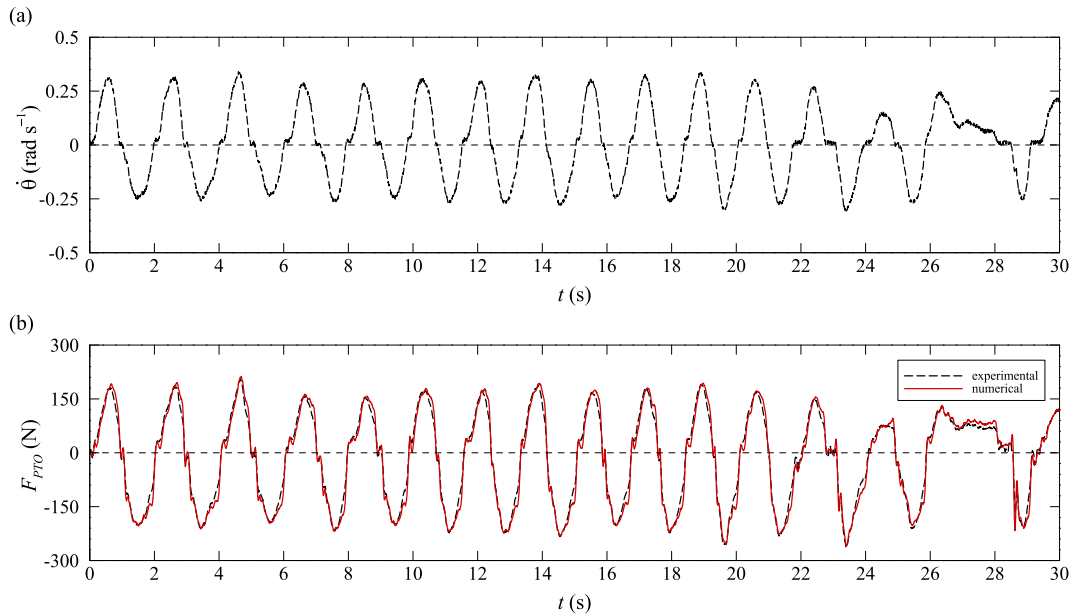


**Fig. 3.** Time series: (a) imposed angular velocity of the flap [49]; (b) comparison of the numerical and experimental PTO force.

lower  $\varphi_x$  was obtained and therefore the Project Chrono is assumed as capable to predict OWSC dynamics, and thus the full mechanical modelling of flap-mechanical system interaction.

### 3.2. Wave generation and propagation

In this section the experimental tests described in Ref. [21] are used here for the validation of the numerical simulation tool. The wave flume was approximately 60 m long (wave direction), 1.5 m wide and 1.8 m deep, and was equipped with a piston-type wavemaker. At the end of the wave flume, there was a passive beach with longitudinal slope of 3:10. The bed and the sidewalls of the wave

flume were made of polished concrete. A schematic sketch of the wave flume is shown in Fig. 4.

In order to validate the wave generation and propagation and to

**Table 2**  
Regular wave conditions considered for the validation of wave generation and propagation.

Test	$d$ (m)	$T$ (s)	$H$ (m)	$\lambda$ (m)
R1	0.825	2.0	0.15	4.90
R2	0.825	2.0	0.25	4.90
R3	0.825	3.0	0.20	8.01
R4	0.825	3.5	0.25	9.51

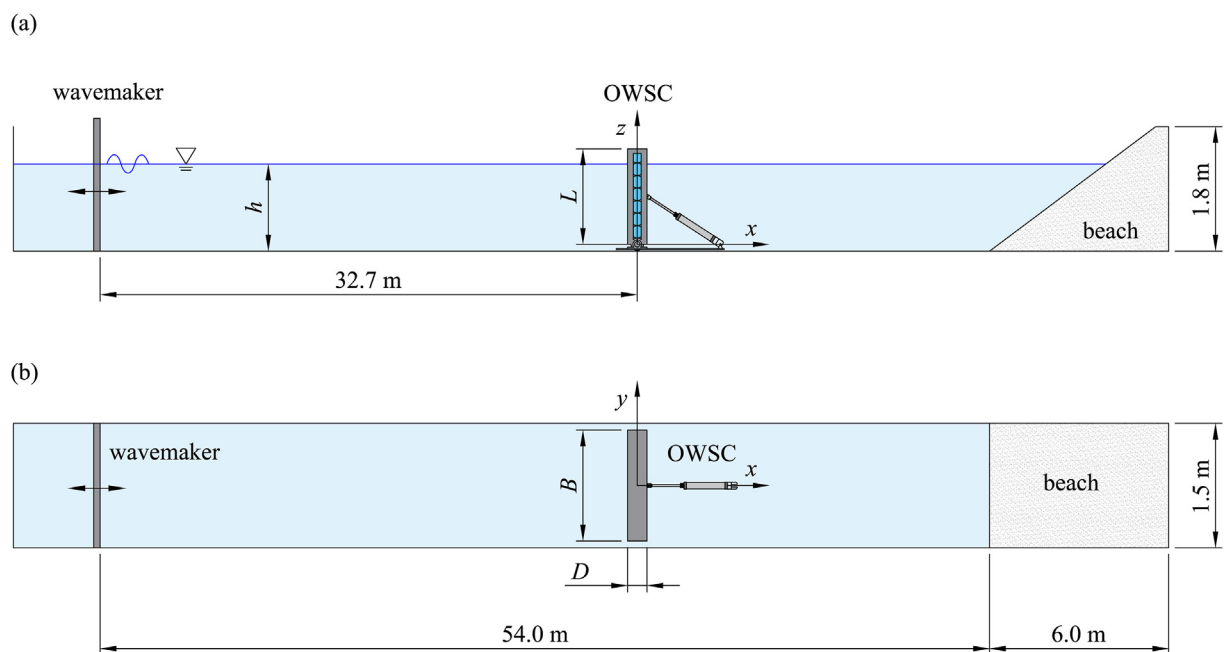


**Fig. 4.** Schematic sketch (not to scale) of the wave flume: (a) side view; (b) plan view.

**Table 3**

Irregular wave conditions considered for the validation of wave generation and propagation.

Test	$d$ (m)	$T_p$ (s)	$H_s$ (m)	$H_m$ (m)
I1	0.825	3.6	0.25	0.15
I2	0.825	2.5	0.2	0.12

**Table 4**

Comparison of the parameters for different resolutions for the test R1 in 2D.

$d_p$ (m)	particles	particles/ $H$	runtime (min)	$A_\chi$	$\varphi_\chi$
0.005	2,217,430	30	14,850	0.99	0.15
0.008	866,737	19	3920	0.99	0.17
0.01	554,977	15	2100	0.98	0.18
0.02	138,806	8	340	0.96	0.21
0.04	34,824	4	70	0.86	0.36
0.05	22,290	3	50	0.80	0.42

study the convergence analysis, experimental and numerical tests were performed removing the OWSC model from the wave flume. The validation is firstly carried out for four regular wave conditions

with still water depth,  $d$ , wave period,  $T$ , wave height,  $H$ , and wavelength,  $\lambda$ , presented in Table 2.

To validate the numerical simulation tool for more realistic applications, numerical tests were also carried out for irregular waves, generated by two standard JONSWAP (Joint North Sea Wave Observation Project) spectrum with peak enhancement factor of 1.2. The considered peak period,  $T_p$ , significant wave height,  $H_s$ , and mean wave height,  $H_m$ , are given in Table 3.

A convergence analysis has been carried out for the test R1 in 2D, where different resolutions (i.e., different initial interparticle distance,  $d_p$ ) are used to obtain the free-surface elevations,  $\eta$ . The total number of particles, computational runtime, number of particles per  $H$ ,  $A_\chi$  and  $\varphi_\chi$  for each  $d_p$  are given in Table 4.

It can be observed that for  $d_p \leq 0.01$  m,  $A_\chi \approx 1$  was obtained, which means a good agreement between numerical results and experimental data. Also, lower  $\varphi_\chi$  is achieved when decreasing  $d_p$  (increasing resolution). However,  $d_p = 0.01$  m (approximately 15 particles per  $H$ ) was shown to be accurate enough to simulate  $\eta$  with relative low computational runtime about 2100 min of 300 s of physical time. Simulations have been executed on a Nvidia GTX 1060. This is in line with [50,51] who have proposed that more than 10 particles per  $H$  allows for the modelling of wave propagation

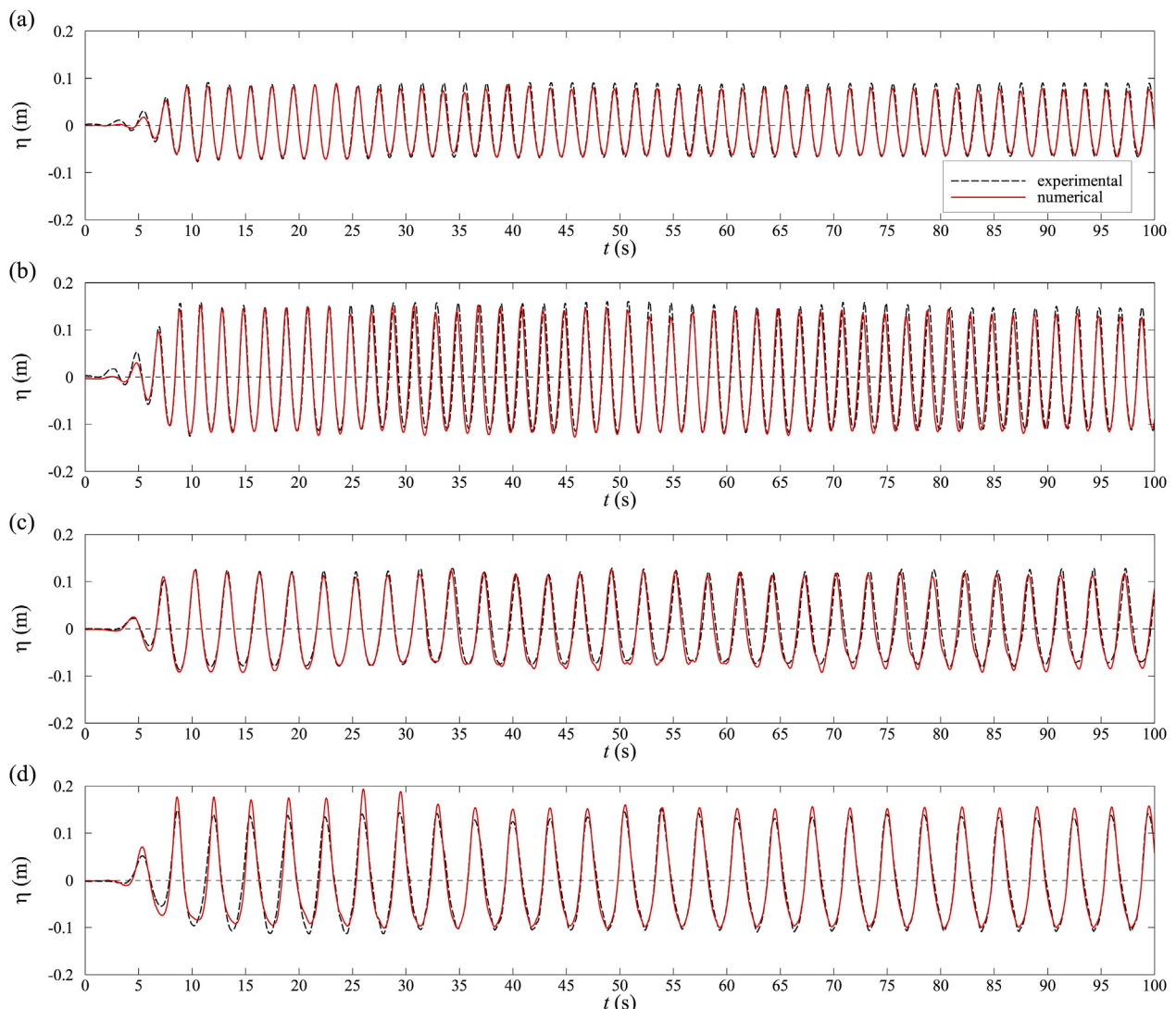


**Fig. 5.** Comparison of the numerical and experimental time series of free-surface elevation in 2D for test: (a) R1; (b) R2; (c) R3; (d) R4.

**Table 5**

Statistical parameters of wave generation and propagation, and comparison of the mean reflection coefficient in 2D.

Test	$A_\chi$	$\varphi_\chi$	experimental $\epsilon$	numerical $\epsilon$	relative error of $\epsilon$
R1	0.98	0.18	8.6%	8.1%	5.8%
R2	0.97	0.19	11.8%	12.6%	6.8%
R3	1.02	0.22	13.3%	14%	4.4%
R4	1.04	0.21	12.6%	13.2%	4.8%

with a good accuracy (i.e., with  $A_\chi \approx 1$  and  $\varphi_\chi < 0.25$ ). The validation of the wave generation and propagation was then carried out in 2D with  $d_p = 0.01$  m. The comparison of the experimental and numerical time series of  $\eta$  obtained at  $x = 0$  (i.e., 32.7 m from the wavemaker) is shown in Fig. 5.

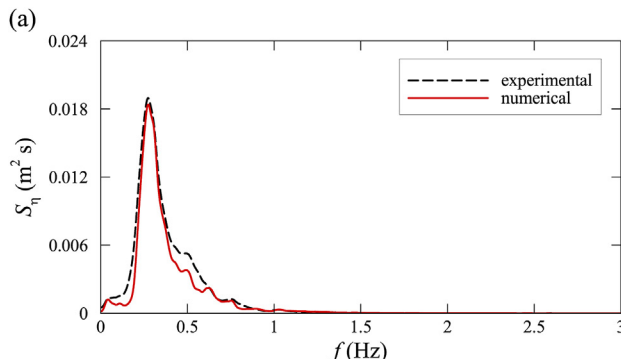
In general, a good agreement between numerical and experimental time series of  $\eta$  are obtained for all wave conditions, with  $A_\chi \approx 1$  and  $\varphi_\chi < 0.25$  (see Table 5). The mean reflection coefficient,  $\epsilon$ , of each numerical test are very similar to the experimental data. The separation of incident and reflected waves was obtained using the method proposed by Ref. [52]. The low relative error between experimental and numerical results of  $\epsilon$  confirms that the waves are being properly generated and propagated.

Fig. 6 shows the power spectral density function of free-surface elevation,  $S_\eta$ , obtained at  $x = 0$  for both irregular tests (Table 3). The power spectral density function describes the distribution of power associated to the time-series across frequencies. It is computed using a fast Fourier transform (FFT) algorithm. To get accurate results, more than 1000 frequencies were calculated in the interval  $f \in [0, 3]$  Hz. It can be observed that the irregular waves are also accurately predicted by the numerical simulation tool. Comparing the peak values, a higher relative error of about 4% was found between both tests. For the relatively higher frequency,  $S_\eta$  shows that the maximum relative error is of about 20%. This difference may be attributed to the viscous dissipation effects of SPH method that occurs for relatively higher frequencies.

The simulation of the full 3D wave flume (Fig. 4) with about 10 particles per  $H$  requires more than 84 millions of particles, leading to an impracticable computational time. For this reason, the length of the computational domain need to be reduced. However, the reduction of the domain length may cause different reflections at boundaries and leads to unphysical behavior of waves [23]. To evaluate the effect of the domain length on the results, several 2D simulations were performed for tests R1 and I1.

The total number of particles, computational runtime,  $A_\chi$  and  $\varphi_\chi$  for different domain length are given in Table 6. The value of  $A_\chi$  and  $\varphi_\chi$  were obtained comparing each domain length with full wave flume.

Fig. 7 shows the  $S_\eta$  with different domain length for test I1 in 2D.

**Table 6**

Comparison of the parameters with different domain length for the test R1 in 2D.

Domain length	particles	runtime (min)	$A_\chi$	$\varphi_\chi$
full wave flume	554,977	2100	—	—
$6\lambda$	365,882	1300	1.01	0.04
$3\lambda$	174,941	600	1.05	0.06
$\lambda$	47,647	160	1.31	0.42

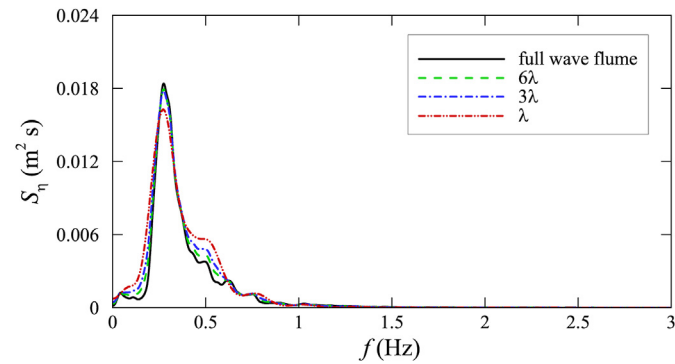


Fig. 7. Comparison of the power spectral density function of free-surface elevation with different domain length for test I1 in 2D.

It is observed that the computational domains with length larger than  $3\lambda$  show a good agreement with full wave flume. A relative error of  $\epsilon$  less than 10% was found. Similar results were obtained by Ref. [23] and [51]. For a longer time simulation and smaller computational domain, special domain treatment like active wave absorption system in the generation of waves should be considered to avoid unphysical behavior of waves.

### 3.3. Hydrodynamics of the OWSC

The OWSC model is attached to the foundation via bearings with its horizontal axis at 0.10 m above the flume bed and a total gap of

**Table 7**

Comparison of the parameters with different resolutions for tests R4 and I1 in 3D.

$d_p$ (m)	million particles	runtime (hours)	test R4		test I1	
			$A_\chi$	$\varphi_\chi$	$A_\chi$	$\varphi_\chi$
0.008	69.8	634	0.98	0.16	0.97	0.17
0.009	48.3	385	0.98	0.16	0.97	0.18
0.01	31.5	246	1.02	0.21	0.96	0.22
0.012	18.6	161	0.94	0.24	0.96	0.28
0.014	11.4	105	0.85	0.41	0.83	0.36

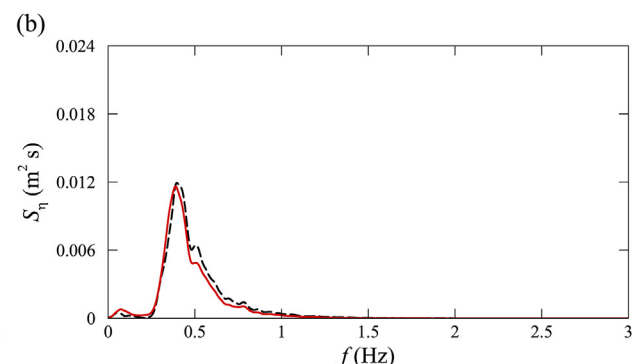
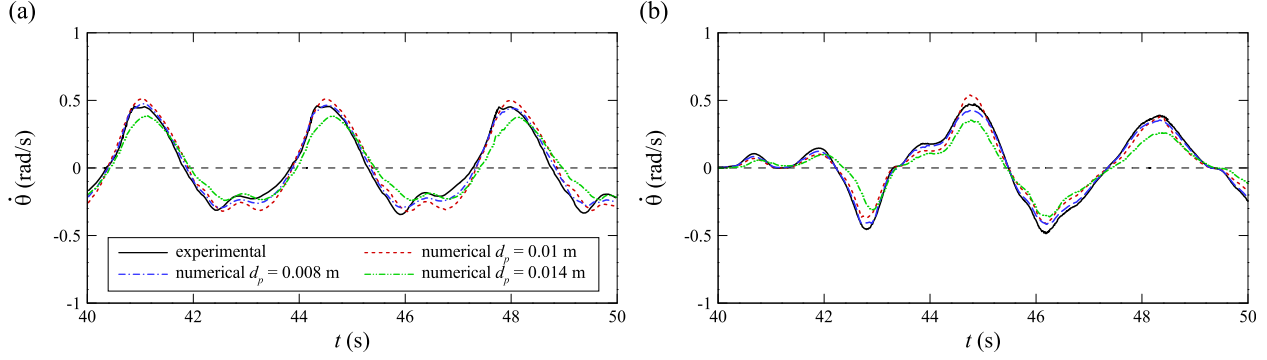
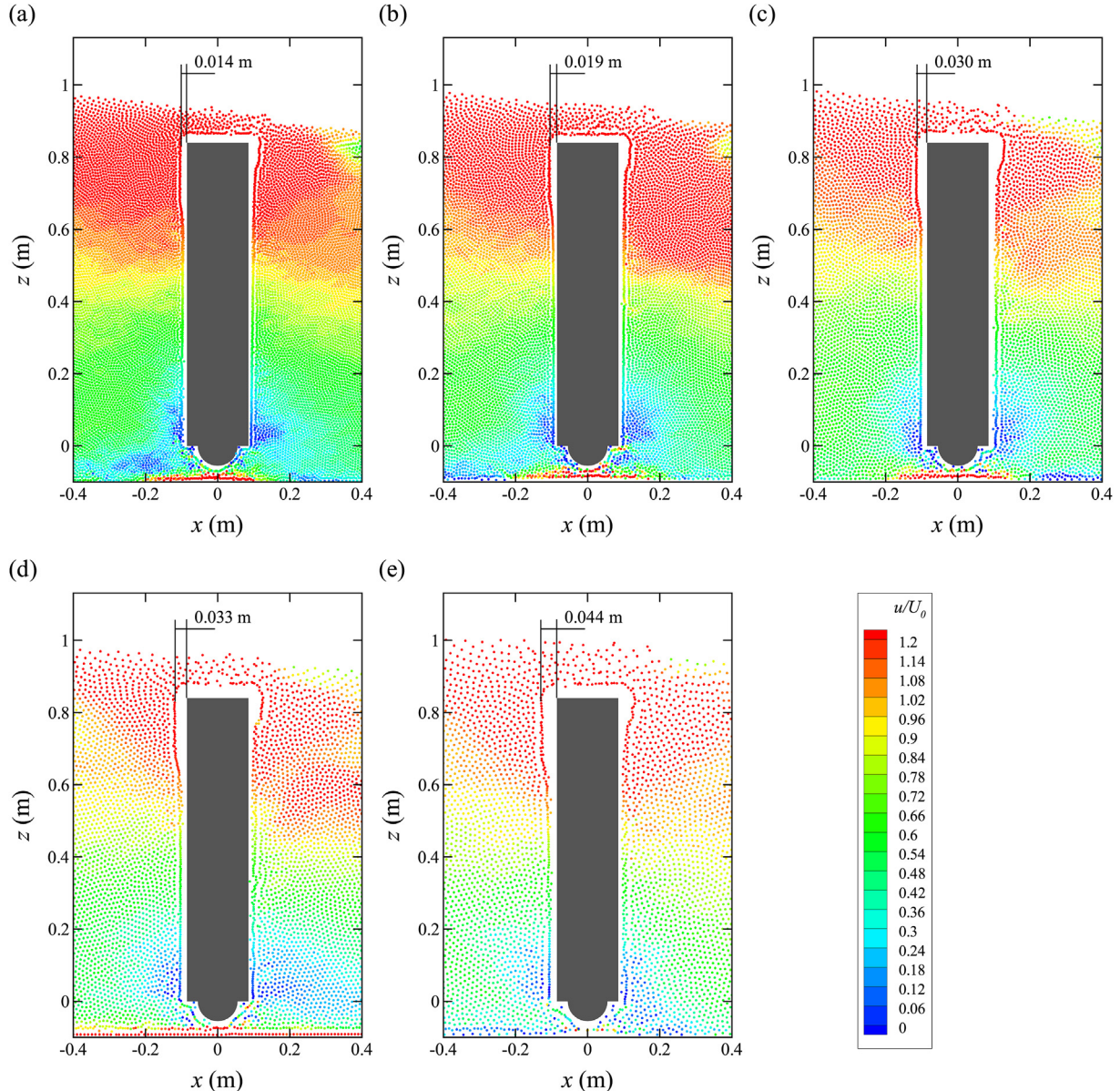


Fig. 6. Comparison of the numerical and experimental power spectral density function of free-surface elevation for test: (a) I1; (b) I2.



**Fig. 8.** Comparison of the time series of angular velocity with different resolutions ( $d_p = 0.008, 0.009, 0.01, 0.012$  and  $0.014$  m) for test: (a) R4; (b) I1.



**Fig. 9.** Comparison of the velocity field in the vicinity of OWSC with different resolutions when the wave crest begins to pass over the flap: (a)  $d_p = 0.008$  m; (b)  $d_p = 0.009$  m; (c)  $d_p = 0.01$  m; (d)  $d_p = 0.012$  m; (e)  $d_p = 0.014$  m.

9.5 cm between the lateral sides of the flap and the sidewalls of the flume (see Fig. 4). The hydrodynamics of the OWSC model are validated in 3D computational domain with wave flume length of  $3\lambda$ , for the regular (R1, R2, R3 and R4) and irregular waves (I1 and I2). To prevent the penetration of fluid particles across the floating body the flap was filled with boundary particles.

In order to study the effect of spatial resolution on the hydrodynamic of the OWSC, simulations have been carried out for tests R4 and I1 in 3D with  $d_p = 0.008, 0.009, 0.01, 0.012$  and  $0.014$  m. Due to the large computational time, the simulations were performed for 50 s of physical time on a Nvidia GTX 2080 alongside with an Intel Xeon E5, allowing for large number of particles to be stored. The total number of particles, computational runtime,  $A_\chi$  and  $\varphi_\chi$  for each  $d_p$  are given in Table 7.

For  $d_p \leq 0.01$  m, the value of  $A_\chi$  for both tests are close to unity showing the good agreement between the numerical results and the experimental data. In the same way, lower  $\varphi_\chi$  is achieved when increasing resolution. The comparison of  $\dot{\theta}$  with different resolutions are presented in Fig. 8. As expected, the results show that the best results are obtained using the highest number of particles. This implies the convergence of the numerical model when increasing the resolution.

Fig. 9 shows the instantaneous velocity field of  $u$  with different resolutions in the plane  $x - z$  and at the middle section of the flume ( $y = 0$ ) when the wave crest begins to pass over the flap ( $\theta \approx 0$ ). These velocity fields correspond to the test R4 and were normalised by the deep-water maximum particle velocity,  $U_0 = \pi H/T$ , being  $U_0 = 0.22$  m s<sup>-1</sup>. It is shown that the larger  $d_p$  leads to the greater gap (e.g., for  $d_p = 0.008$  m the gap is of about 0.014 m and for  $d_p = 0.014$  m the gap is of about 0.044 m). With the increasing of spatial resolution the velocity field is captured more accurately. This confirms that increasing the resolution will improve the accuracy of the simulation.

Since the resolution  $d_p = 0.01$  m can produce reliable results, this resolution is used in the following simulations. Fig. 10 shows the comparison of the numerical and experimental time series of  $\dot{\theta}$  for regular waves (Table 2). These simulations were performed for 100 s of physical time. It can be observed that the numerical  $\dot{\theta}$  shows a small deviation from the experimental data, which may be caused by the superposition of the reflected and incident waves. However, the numerical simulation tool can predict most of OWSC dynamic with a satisfactory accuracy ( $A_\chi \approx 1$  and  $\varphi_\chi < 0.25$ ).

The experimental and numerical power spectral density functions of the free-surface elevation,  $S_\eta$ , obtained in the middle of the

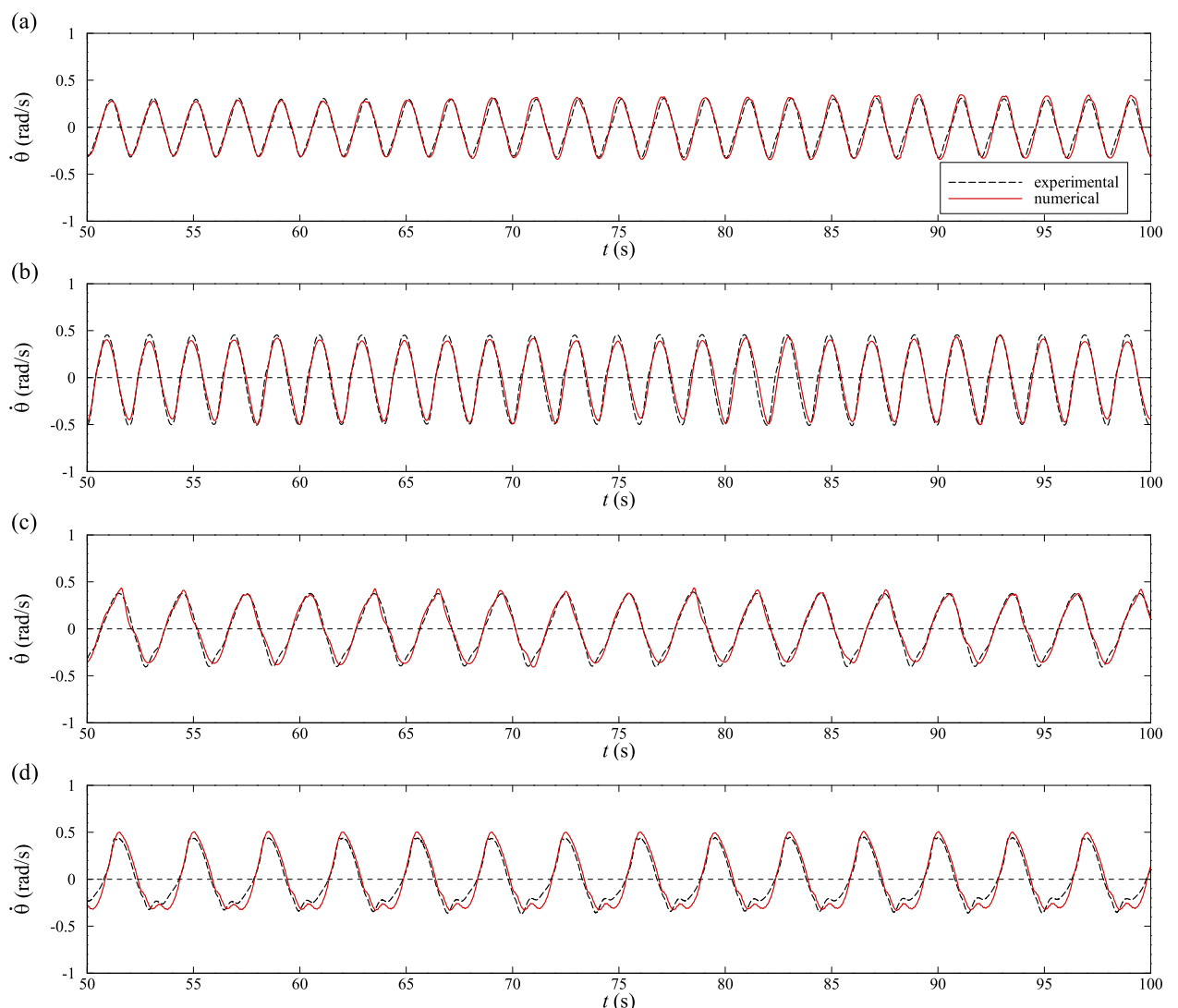


**Fig. 10.** Comparison of the numerical and experimental time series of angular velocity of the flap for test: (a) R1; (b) R2; (c) R3; (d) R4.

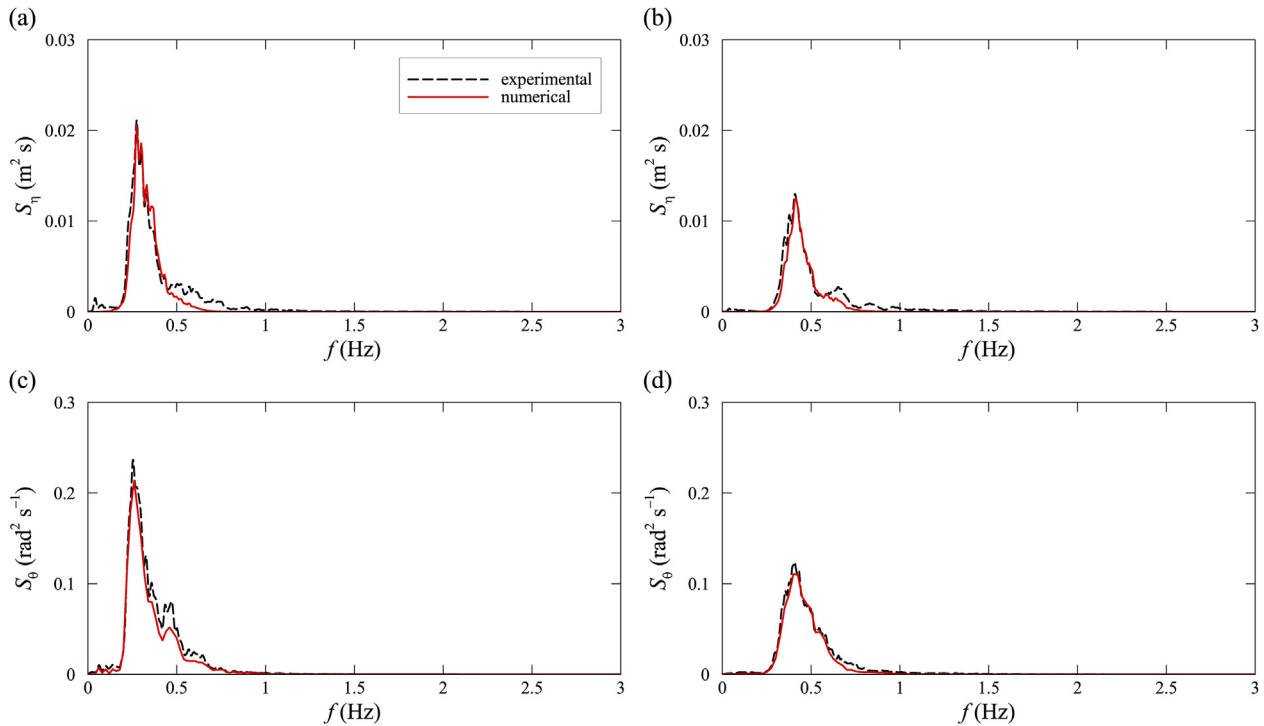


**Fig. 11.** Comparison of the numerical and experimental power spectral density function of free-surface elevation and angular velocity of the flap for test: (a,c) I1; (b,d) I2.

flume ( $y = 0$ ) at  $x = -3.43$  m, and of angular velocity of the flap,  $S_{\dot{\theta}}$ , for both tests I1 and I2 are compared in Fig. 11. These simulations are also performed in 3D.

Comparing the peak values of  $S_{\eta}$ , a relative error of about 4% was found between the tests (similar to Fig. 6). The peak values of  $S_{\dot{\theta}}$  for both tests I1 and I2 shows a relative error of about 10%. For a relatively higher frequencies the  $S_{\eta}$  shows greater difference with maximum relative error of about 20%. However, in general, it can be observed that both  $S_{\eta}$  and  $S_{\dot{\theta}}$  are accurately predicted by the numerical simulation tool.

#### 3.4. Phase-averaged flow field

The flow velocity was measured using an ultrasonic velocity profiler (UVP) produced by Ref. [53] in the centre plane of the wave flume ( $y = 0$ ). The measurements of longitudinal and vertical velocity components were performed for the test R4 using three UVP probes (UP1, UP2 and UP3) pointing in different directions. The probes were fixed at  $x = -(0.16 + D/2)$  m and an angle  $\alpha = 30^\circ$  between UP1, UP3 and horizontal is considered. The UVP was operated with a sample frequency of 11.6 Hz and a Doppler frequency of 2 MHz. As UVP measures velocities along one line in space, the velocity field was obtained by repeating the same test 78 times and moving the probes across the vertical direction with step of 2 cm (from  $z = 0.20$  to 0.72 m). The velocity field is obtained by phase-averaging the velocity signal over 50 successive waves for the half wave cycle with  $\theta > 0$  [54,55]. The phase-averaged velocity vector fields,  $(\langle u \rangle \langle w \rangle)$ , normalised by  $U_0$  at different phase when the flap moves toward the beach ( $\theta > 0$ ) are compared in Figs. 12 and 13.

A small difference in the orientation of vectors near the flume bed and near the free-surface are observed between experimental data and numerical results. The experimental ascendant flow, caused by the approach of the wave crest and the blockage effect of the flap, is mostly larger than the numerical one. The experimental

$\langle w \rangle$  component is mostly larger than the numerical one near the free-surface. The  $\langle u \rangle$  component in the recirculation zones is roughly estimated, due to the presence of longitudinal and vertical gradients, related to the deceleration of the flow caused by the reversal motion of the flap. In general, the magnitudes of  $(\langle u \rangle \langle w \rangle)$  fields were predicted with reasonable accuracy. It is difficult to identify the vortex caused by the flap deceleration in the experimental data, due to the limited size of the measurement mesh. However, the numerical results provide a full flow field in the vicinity of the flap. The main limitation of these results is the gap (with a maximum value of about 0.03 m) between fluid and flap near the freeboard.

## 4. Numerical analysis of the hydrodynamics of OWSC

The new numerical simulation tool presented in Section 2 and validated in Section 3 is here applied to study the influence of the mechanical constraints, PTO system coefficients and flap inertia on the hydrodynamic of the OWSC under regular waves. These analyses were performed for the wave test conditions R1 and R2 (Table 2).

### 4.1. Influence of mechanical constraints

To explore the influence of mechanical constraints on the hydrodynamics of the OWSC five different cases are considered. In the first case (C1) all mechanical constraints characterized experimentally in Ref. [49] were considered, i.e., the static friction coefficient on the revolute joint between flap and bearings is 0.16,  $F_p$  and  $F_f$  are given according to Appendix A and Appendix B, respectively. Regarding the relevance of  $F_f$ , the second case (C2) was done with the above mechanical constraints and with  $F_f = 0$ . Similar to C2, the third case (C3) was performed with  $F_p = 0$ . The fourth case (C4) was done without PTO system (i.e.,  $F_p = 0$  and  $F_f = 0$ ) and with the friction torque on the revolute joint between flap

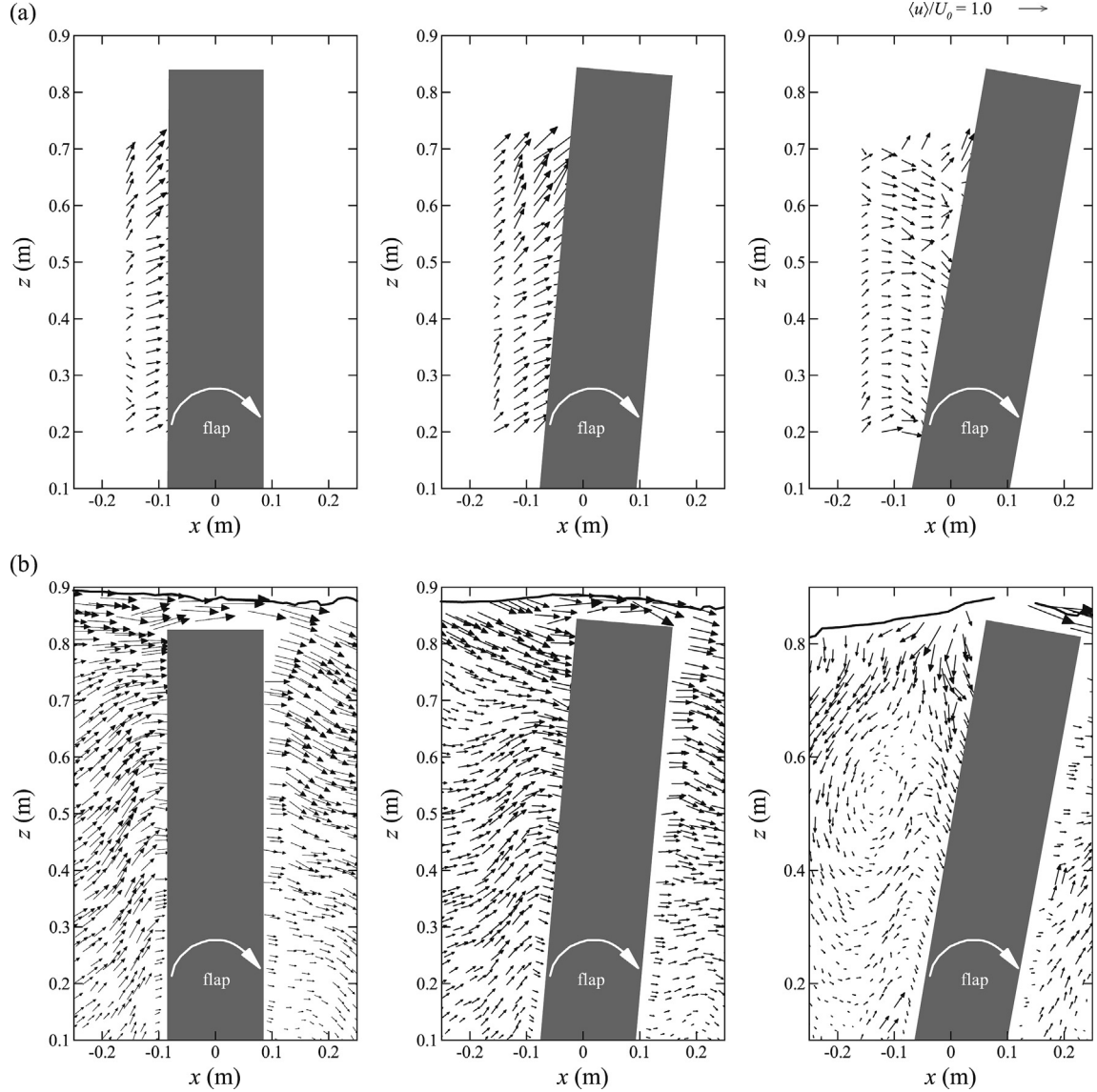


**Fig. 12.** Comparison of the velocity field in the vicinity of OWSC for  $\dot{\theta} > 0$ : (a) experimental; (b) numerical.

and bearings. As a reference situation, the fifth case (C5) was done without friction torque on the revolute joint between flap and bearings and with PTO system. The time series of  $\dot{\theta}$  and the hydrodynamic moment around the bearings,  $T_h$ , for the described mechanical constraints are compared in Figs. 14 and 15.

As expected, mechanical constraints have a non-negligible influence on the hydrodynamics of OWSC. It can be observed in Fig. 14 that both  $F_p$  and  $F_f$  have an important effect on the  $\dot{\theta}$  and  $T_h$ . The influence of  $F_p$  is more relevant to the response amplitude of the OWSC than that of  $F_f$ . For the test R1, the maximum amplitude of  $\dot{\theta}$  in test case C3 is approximately 50% larger than C1 (Fig. 14a), while for the test R2 is approximately 70% (Fig. 14b). For C2 case these differences are less than 10% for both tests. This behavior is caused by larger damping effect of  $F_p$ . Without this damping effect (case C3) a larger fluctuations of  $T_h$  are observed. In contrast,  $F_f = 0$  causes a phase difference between C1 and C2. Similar effect (between C1 and C5) is induced by the friction torque on the revolute joint between flap and bearings (Fig. 15). Without friction torque on the revolute joint between flap and bearings and with PTO system (C4), the flap basically follows the wave.

#### 4.2. Influence of PTO damping coefficients

The influence of the PTO system on the hydrodynamics of OWSC is analyzed through the change of its damping coefficients. From the several coefficients of  $F_p$  and  $F_f$  (see Appendix A and Appendix B), the pressure loss coefficient,  $K_p$ , and viscous friction coefficient,  $\sigma_2$ , are seen to be the most relevant on the power capture. The value of  $K_p$  depends on the flow conditions in the hydraulic circuit, while  $\sigma_2$  depends on the deformation characteristics of the rod bristles (made of rubber). The analysis was performed for ten values of  $K_p$  ranging from  $3.25 \times 10^5$  to  $16.25 \times 10^5$  Pa s<sup>2</sup> and for seven values of  $\sigma_2$  ranging from 100 to 1000 N s m<sup>-1</sup>. The analysis of  $K_p$  effect was done for constant  $\sigma_2 = 300$  N s m<sup>-1</sup> and the analysis of  $\sigma_2$  effect was performed for constant  $K_p = 6.5 \times 10^5$  Pa s<sup>2</sup>. The set  $\sigma_2$  and  $K_p$  are the reference experimental values obtained by Ref. [49].

An example of the time series of  $\dot{\theta}$  and the instantaneous power capture,  $W_{out}$ , for three different PTO damping coefficients is presented in Fig. 16.

The results highlight that the designer should be worried with rate-dependent deformation characteristics (viscoelastic nature) of

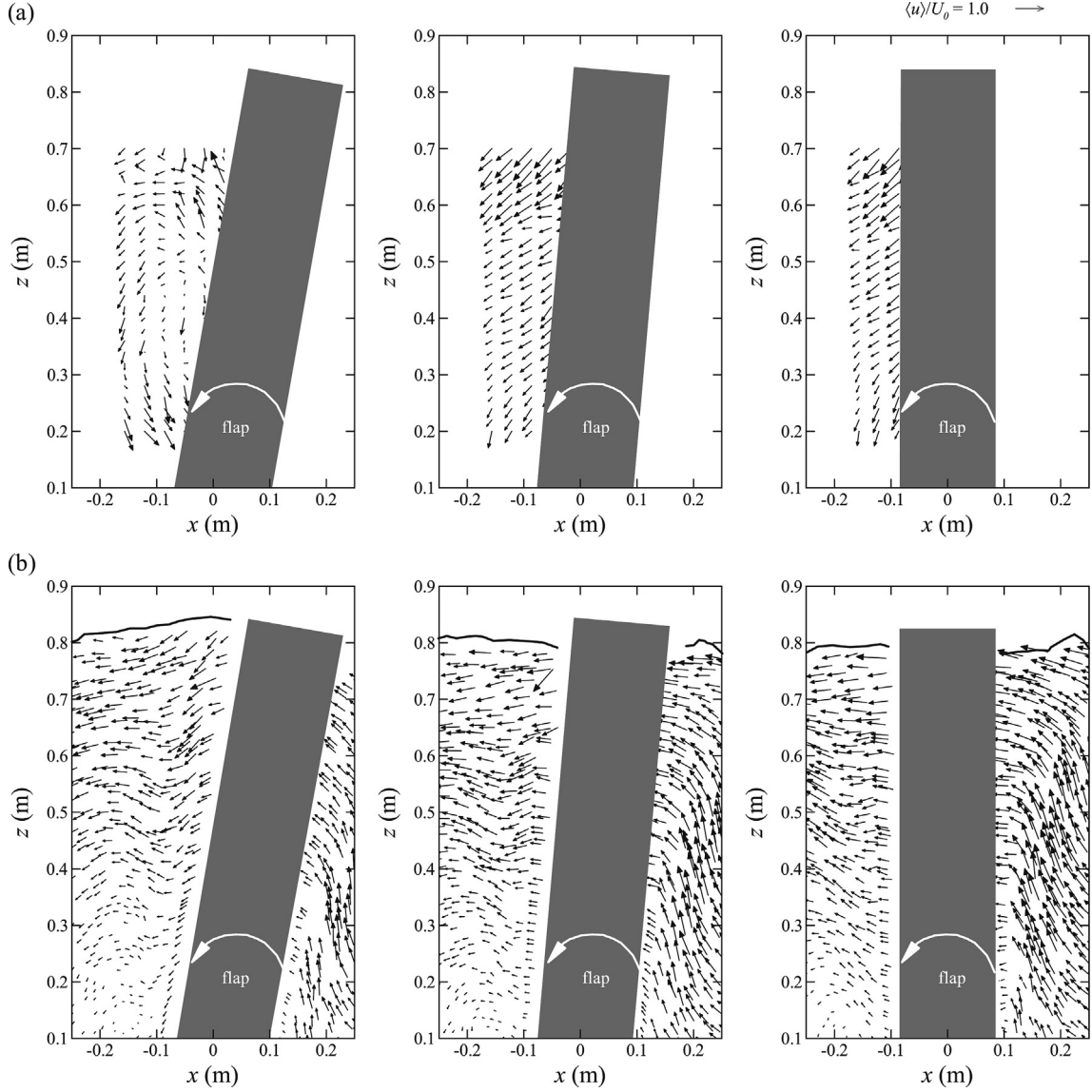


**Fig. 13.** Comparison of the velocity field in the vicinity of OWSC for  $\bar{\theta} < 0$ : (a) experimental; (b) numerical.

the rubber and not with pipe diameter and roughness, as the  $W_{out}$  varies a lot with  $\sigma_2$  and not  $K_p$  (see Fig. 16c and d). The main consequence of this result is the large modification of the capture width ratio (CWR) of the OWSC, defined as the ratio of mean power capture,  $\overline{W}_{out}$ , and mean incident power,  $\overline{W}_i$ :

$$\text{CWR} = \frac{\overline{W}_{out}}{\overline{W}_i} \quad (16)$$

According to the linear theory, for unidirectional regular waves the mean incident power is given by:

$$\overline{W}_i = \frac{1}{8} \rho g H^2 c_g B \quad (17)$$

where  $c_g$  is the wave group velocity. For the intermediate water depth wave conditions,  $c_g$  is given by:

$$c_g = \frac{\omega}{2k} \left( 1 + \frac{2kh}{\sinh 2kh} \right) \quad (18)$$

where  $\omega = 2\pi f$  is the wave angular frequency,  $f$  is the wave frequency and  $k$  is the wavenumber, given by the dispersion relationship  $\omega^2 = gk \tanh(kh)$ .

The mean power capture is determined as:

$$\overline{W}_{out} = \frac{1}{t_{total}} \int_0^{t_{total}} F_p(t) \dot{x}(t) dt \quad (19)$$

where  $t_{total}$  is the duration of the test and  $\dot{x}$  is the linear relative velocity between piston rod and cylinder body.

The variation of CWR with  $\sigma_2$  and  $K_p$  is presented in Fig. 17. It can be seen that the variation of both damping coefficients have important effects on the CWR. The influence of  $\sigma_2$  is more relevant than  $K_p$  for the same ratio of variation. In fact, CWR decreases significantly with increasing of  $\sigma_2$  and a much smaller difference is

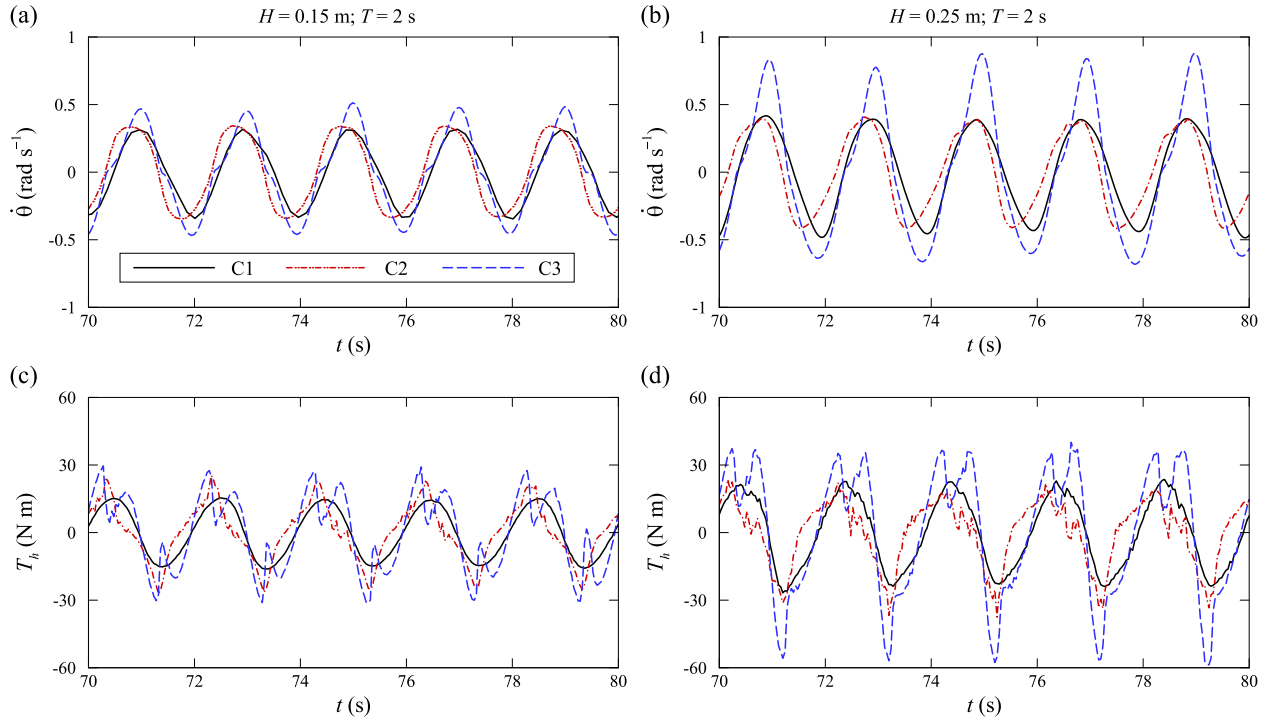


**Fig. 14.** Influence of mechanical constraints (C1, C2 and C3) on the: (a,b) angular velocity of the flap; (c,d) hydrodynamic moment around the bearings.

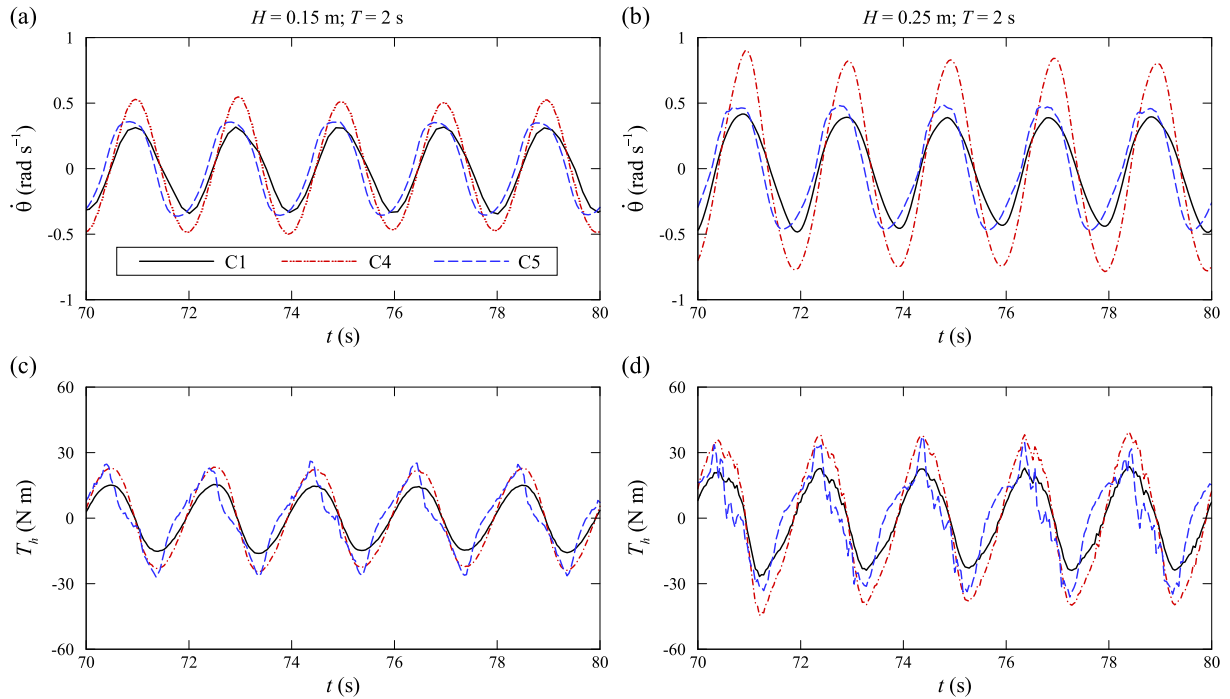


**Fig. 15.** Influence of mechanical constraints (C1, C4 and C5) on the: (a,b) angular velocity of the flap; (c,d) hydrodynamic moment around the bearings.

shown with increasing of  $K_p$ . The influence of the  $\sigma_2$  presents a maximum difference in the CWR of about 200% for both tests (Fig. 17a). While  $K_p$  shows a maximum difference of about 20% for the test R1 and 50% for test R2 (Fig. 17b). This behavior is caused by the large energy dissipation through the  $\sigma_2$  and the notable change in the flow field (i.e., available energy) caused by its brake effects.

In order to illustrate the influence of these parameters on the

flow field, Fig. 18 shows the instantaneous velocity fields for the three different PTO damping coefficients presented in Fig. 16, at  $t = 52, 52.5, 53$  and  $53.5 \text{ s}$ . These velocity fields correspond to the test R2. The different mechanical moment (applied by the PTO system on the flap) causes a large variation on the velocity field, including a strong nonlinear behavior. Due to the nonlinearity of the wave-OWSC interaction, a large discrepancy can be observed in the

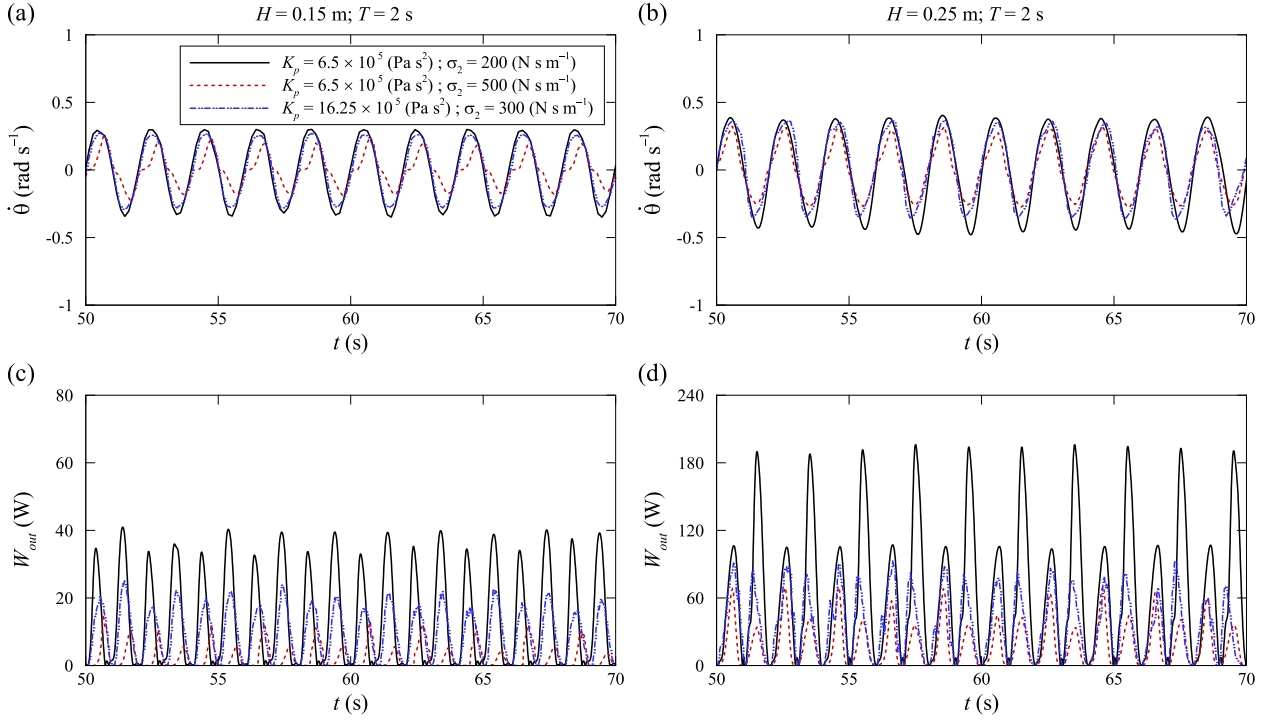


**Fig. 16.** Influence of PTO damping coefficients on the: (a,b) angular velocity of the flap; (c,d) instantaneous power capture.

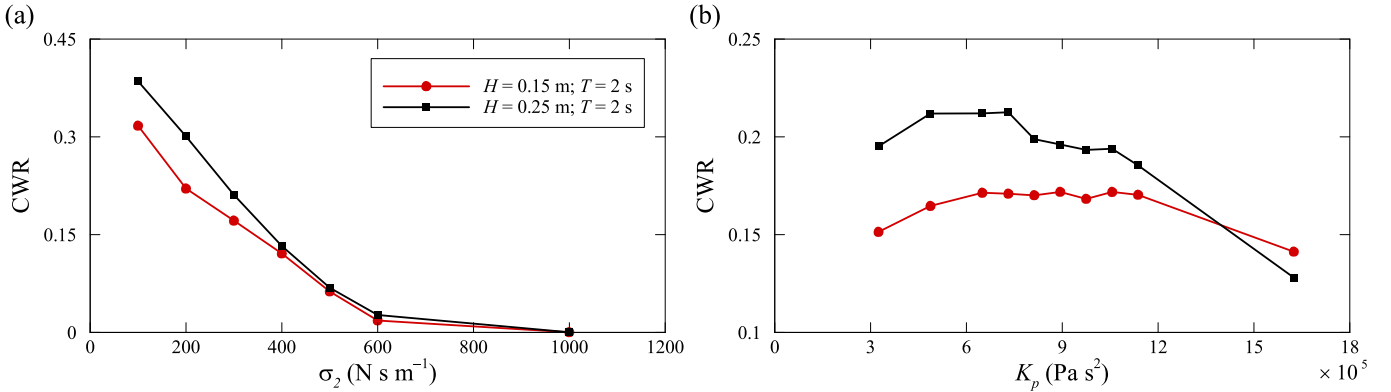


**Fig. 17.** Influence, on the CWR, of the: (a) viscous friction coefficient; (b) pressure loss coefficient.

free-surface elevation and velocity distributions for different PTO damping coefficients. For example, at  $t = 52 \text{ s}$ , when the wave crest starts to approach the flap, different ascendant flows are observed, which are caused by the blockage effect of the flap [56]. Hence, the mass of water that passes over the flap (wave overtopping) at  $t = 52.5 \text{ s}$  is different from case to case, indicating that  $W_{out}$  is affected by the instantaneous submergence of the flap. A different wake is also observed at  $t = 53$  and  $53.5 \text{ s}$ , characterized by the flow rotation, which is irreconcilable with potential flow description.

#### 4.3. Influence of flap inertia

The analysis of the flap inertia influence on the hydrodynamics of the OWSC is performed using a similar technique as presented in Ref. [3]; i.e., in two stages. The first is based on the variation of the flap mass,  $m$ , and its centre of mass,  $\bar{z}$ . The second is based on the variation of the flap height,  $L$ , and thickness,  $D$ . It should be noted that the change of these parameters results in the modification of

the flap moment of inertia. The analysis of  $m$  effect was performed considering that the  $m$  is uniformly distributed over the flap with a constant  $\bar{z} = 0.33 \text{ m}$ . The analysis of  $\bar{z}$  effect is done imposing different values of  $\bar{z}$  for a constant  $m = 72.3 \text{ kg}$ . The analysis of the flap inertia was performed using reference experimental values of  $K_p = 6.5 \times 10^5 \text{ Pa s}^2$  and  $\sigma_2 = 300 \text{ N s m}^{-1}$ .

The variation of CWR with  $\bar{z}$  and  $m$  are shown in Fig. 19. It can be seen that CWR decreases when increasing both  $m$  and  $\bar{z}$ . In general, the  $\bar{z}$  has more influence on the CWR than  $m$ . The effect of  $\bar{z}$  is approximately twice those of  $m$  for the same ratio of variation of  $\bar{z}$  and  $m$ , respectively. The variation of CWR is bounded by  $\bar{z} < 0.5 \text{ m}$  for test R2 and by  $\bar{z} < 0.2 \text{ m}$  for R1. For a small  $\bar{z}$  the OWSC presents a relatively high CWR. The maximum difference of CWR is of about 75% for the test R1 and 32% for R2 (Fig. 19a). The  $m$  presents a maximum difference of the CWR of about 40% and 18% for tests R1 and R2, respectively (Fig. 19b).

The analysis of  $D$  effect was done considering constant  $m = 72.3 \text{ kg}$  and  $\bar{z} = 0.33 \text{ m}$ . The analysis of  $L$  effect was also performed for a

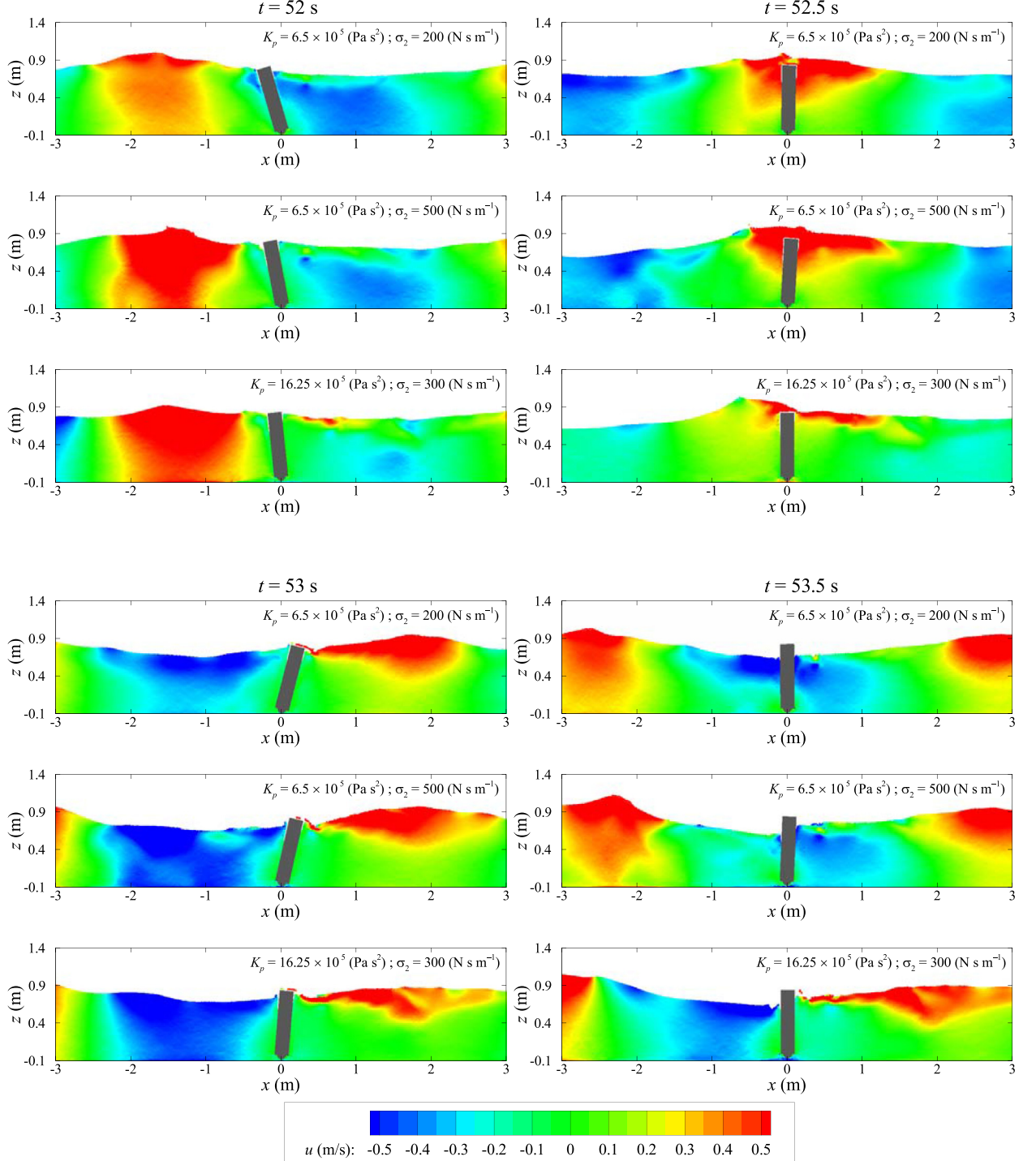


**Fig. 18.** Different instants of the velocity field in the vicinity of the flap for different PTO damping coefficients.

constant  $m$  but considering different values of  $\bar{z}$ , equal to approximately  $0.4L$ . Fig. 20 shows the variation of CWR with  $D$  and  $L$ . The influence of the  $D$  does not seem to be substantial, compared with the influence of the  $L$ . In fact, the CWR slightly increases with increasing of  $D$  (Fig. 20a). In contrast, the  $L$  causes a large variation of the CWR, with its maximum difference of about 160% for both tests (Fig. 20b). This behavior is caused by the changing of the flap submergence ratio that results in a large variation in the wave excitation moment and overtopping.

In order to illustrate the influence of these parameters on the flow field, Fig. 21 shows the instantaneous velocity fields for three different  $L = 0.6, 0.9$  and  $1.1$  m at  $t = 52, 52.5, 53$  and  $53.5$  s. Similar to Fig. 18, these velocity fields correspond to the test R2. The influence of the flap submergence is clearly visible. A very distinct flow features are observed for the fully-submerged ( $L = 0.6$  m) and the surface-piercing flap ( $L = 0.9$  and  $1.1$  m). Such difference is caused by the wave overtopping and flow separation on the freeboard, that have influence only for fully-submerged flap. For

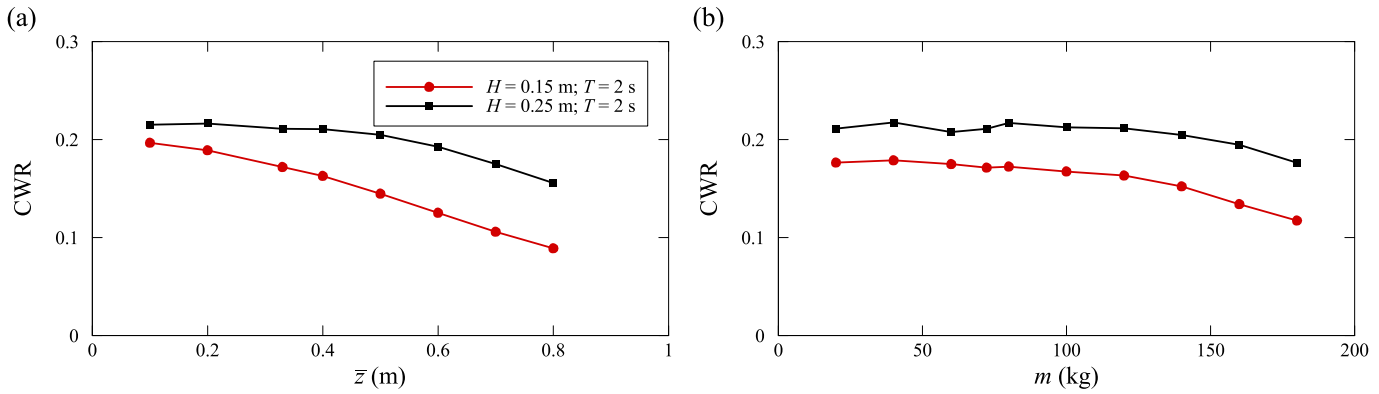


Fig. 19. Influence of the flap inertia: (a) centre of mass; (b) mass.

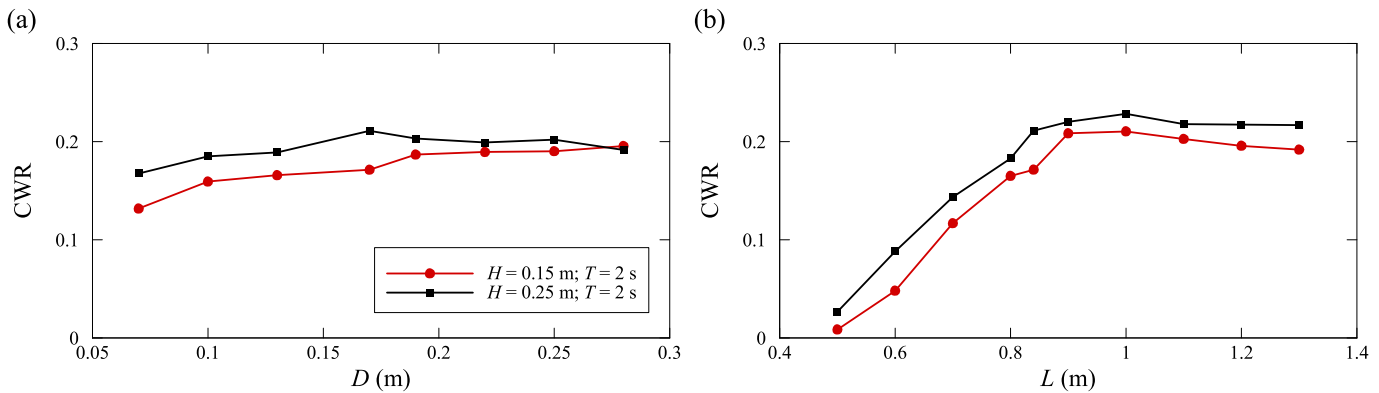


Fig. 20. Influence of the flap inertia: (a) thickness; (b) height.

surface-piercing flap the free-surface elevation and  $u$  distributions seem very similar, resulting in small difference in the CWR (see Fig. 20b).

## 5. Conclusions

A new numerical simulation tool for modelling oscillating wave surge converter (OWSC) with nonlinear mechanical constraints is proposed. It is based on the numerical implementation of the multibody solver of Project Chrono under the Smoothed Particle Hydrodynamics (SPH) model of DualSPHysics code, where the SPH solver resolves wave-flap interaction and the multibody solver resolves flap-mechanical constraints interaction.

The numerical simulation tool was validated using the experimental data of an OWSC with mechanical constraints, including the effects of nonlinear constraints of the hydraulic power take-off (PTO) system and the frictional contacts between flap and bearings. The validation was performed for both unidirectional regular and irregular waves. The comparison between numerical results and experimental data shows that the numerical simulation tool properly predicts the dynamics of the OWSC. Furthermore, the computed and observed free-surface elevation and mean flow field show reasonable agreement, with an amplitude statistical parameter of about 1 and phase-amplitude parameter less than 0.25. The power spectral density functions of the free-surface elevation and of the angular velocity of the flap are also accurately predicted with peak relative errors of about 4% and 10%, respectively. It is shown that the Dynamic Boundary Condition (DBC) does not compromise the description of the system since the solution is shown to improve as the resolution increases. However, would be relevant to

study different boundary conditions, in order to put in perspective the problem of spurious pressure oscillations in the Weakly Compressible SPH (WCSPh) method.

These numerical results demonstrate the capability of the presented numerical simulation tool to be used in the design of OWSCs. It provides a suitable method for modelling wave energy converter (WEC) devices with any mechanical constraints, such as PTO systems, revolute joints, frictional contacts, constraints and sliders.

The validated numerical simulation tool was applied to study the effect of several mechanical constraints, PTO damping coefficients and flap inertia. Mechanical constraints have a non-negligible influence on the hydrodynamics of the OWSC. These constraints exhibit relevant effects on response amplitude and phase of the OWSC. Different mechanical systems can introduce a variation on the response amplitude larger than 50%. The influence of the friction coefficient has shown to be more relevant than that of the pressure coefficient on the capture width ratio (CWR) for the same ratio of variation. The friction coefficient presents a maximum difference in the CWR of about 200%, while pressure coefficient shows a maximum difference of about 50%. This is caused by the large energy dissipation through the friction and the notable change in the available energy caused by its brake effects. Therefore the designer should be concerned with deformation characteristics of the rod bristles and not with hydraulic circuit as the CWR varies a lot with friction and not pressure coefficient.

The effect of the flap inertia was analyzed by changing its mass, centre of mass, height and thickness. The variation of these parameters has relevant effects on the hydrodynamic of OWSC. It was observed that CWR decreases when increasing both flap mass and

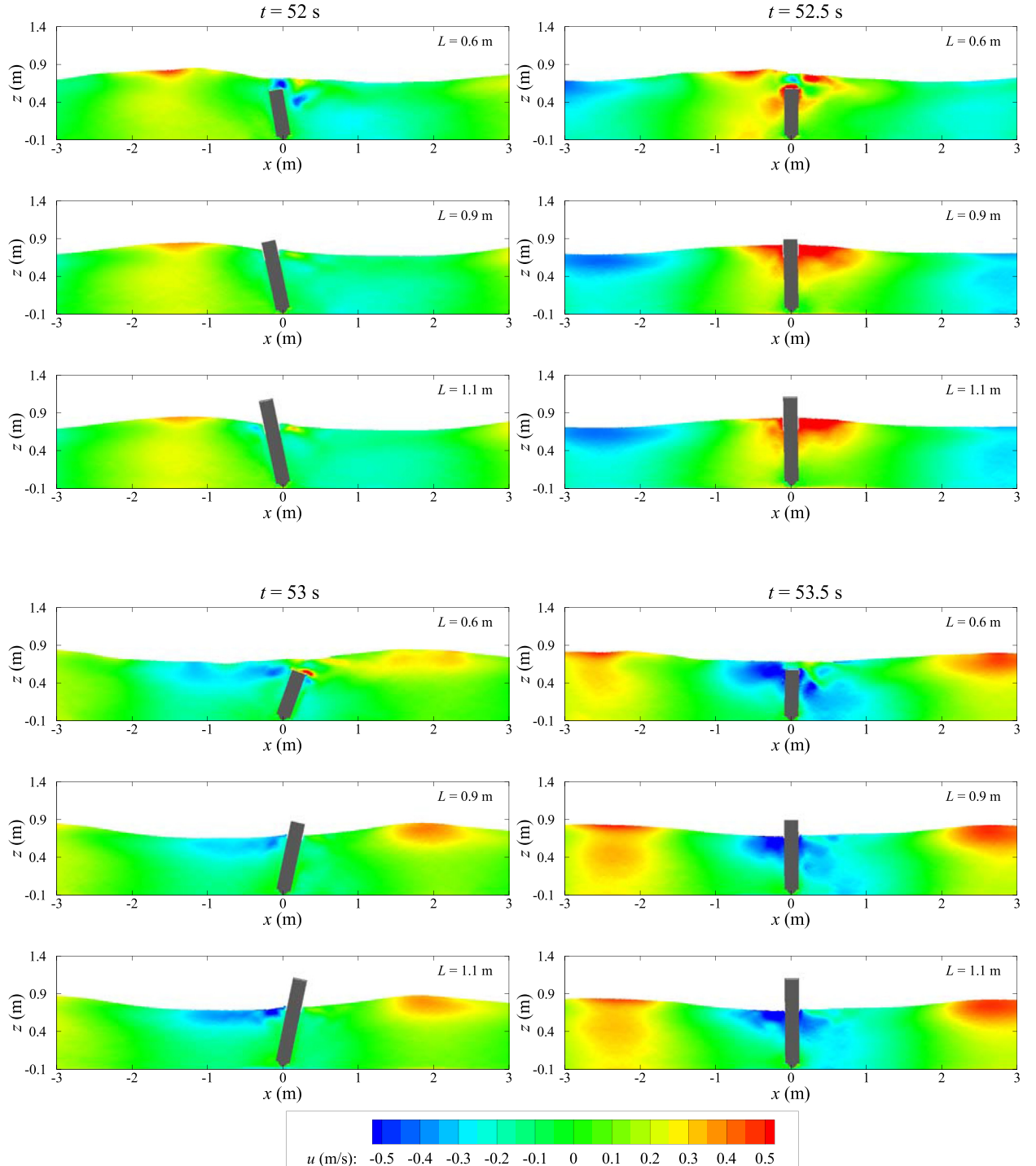


**Fig. 21.** Different instants of the velocity field in the vicinity of the flap for different flap height.

centre of mass. On the other hand, CWR increases when increasing both flap height and thickness, with a much higher dependence on the flap height. Distinct flow trends were observed between the fully-submerged and the surface-piercing flap, generated by the flap freeboard effects.

This methodology followed in this paper features the absolute novelty of using SPH and multi-physics solvers to discuss the configuration of OWSC. This opens the possibility of using these tools in virtual laboratories to aid the design and OWSCs and to test its implementation in field conditions.

## Acknowledgments

The first author acknowledges the support of FCT through the Grant No. PD/BD/705970/2014. This work is also funded by the Ministry of Economy and Competitiveness of the Government of Spain under project WELCOME ENE2016-75074-C2-1-R.

## Appendix A. Pressure force model

The pressure force,  $F_p$ , of the hydraulic cylinder is given by the

following model:

$$F_p = A \begin{cases} K_p \dot{\theta}^2 + I_p \ddot{\theta} & \text{for } \sigma \geq 0 \text{ (no cavitation)} \\ P_v + I_p \dot{\theta} & \text{for } \sigma < 0 \text{ (cavitation)} \end{cases} \quad (\text{A.1})$$

where  $A$  is the cross-section area of the cylinder chamber,  $K_p$  is the coefficient of pressure loss,  $I_p$  is the coefficient that takes into account the inertia of the fluid [49,57],  $P_v$  is the vapor pressure of water in the hydraulic circuit and  $\sigma$  is the Thoma coefficient that allows to determine the cavitation intensity, defined as:

$$\sigma = \frac{P_{atm} + P_{int} - P_v}{P_{atm}} \quad (\text{A.2})$$

## Appendix B. Friction force model

The friction force,  $F_f$ , of the hydraulic cylinder is given by the modified LuGre model [49,58,59]:

$$F_f = \sigma_0 z + \sigma_1 \dot{z} + \sigma_2 \ddot{z} \quad (\text{B.1})$$

and

$$\dot{z} = \dot{x} - \frac{\dot{x}}{g_s(\dot{x}, h_l)} z \quad (\text{B.2})$$

where  $z$  is the mean deflection of the elastic bristles,  $h_l$  is the dimensionless fluid film thickness parameter,  $\dot{x}$  is the linear relative velocity between the piston rod and the cylinder,  $\sigma_0$  and  $\sigma_1$  are the dynamics coefficients, standing for stiffness and micro-viscous friction coefficient of the bristles, respectively. The static coefficient  $\sigma_2$  stands for the viscous friction coefficient. This model takes the Coulomb friction force,  $F_c$ , and Stribeck effect in consideration through the Stribeck function,  $g_s$ , given by:

$$g_s(\dot{x}, h_l) = \frac{1}{\sigma_0} [(1 - h_l) F_c + (F_s - F_c)] e^{-(|\dot{x}|/|\dot{x}_s|)^n} \quad (\text{B.3})$$

where  $h_l$  can be expressed as:

$$h_l = \frac{1}{\tau_h} [h_{ss} - h_l] \quad (\text{B.4})$$

with

$$\tau_h = \begin{cases} \tau_{hp} & \{\dot{x} \neq 0, h_l \leq h_{ss}\} \\ \tau_{hn} & \{\dot{x} \neq 0, h_l > h_{ss}\} \\ \tau_{h0} & \{\dot{x} = 0\} \end{cases} \quad (\text{B.5})$$

$$h_{ss} = \begin{cases} K_f |\dot{x}|^{2/3} & \{|\dot{x}| \leq |\dot{x}_b|\} \\ K_f |\dot{x}_b|^{2/3} & \{|\dot{x}| > |\dot{x}_b|\} \end{cases} \quad (\text{B.6})$$

$$K_f = \left(1 - \frac{F_c}{F_s}\right) |\dot{x}_b|^{2/3} \quad (\text{B.7})$$

where  $h_{ss}$  is the dimensionless steady-state of  $h_l$ ,  $K_f$  is the proportional constant,  $\dot{x}_b$  is the velocity at which the steady-state of  $F_f$  becomes minimum,  $\dot{x}_s$  is the Stribeck velocity,  $n$  is the exponent of  $g_s$  curve,  $F_s$  is the maximum static friction force and  $\tau_{hp}$ ,  $\tau_{hn}$ , and  $\tau_{h0}$  are the time constants for acceleration, deceleration, and dwell periods, respectively. In Equation (B.5),  $h_l < h_{ss}$  corresponds to the

acceleration period,  $h_l > h_{ss}$  to the deceleration period. It is assumed by Equation (B.6) that the  $h_l$  is increased with  $\dot{x}$  only in the negative resistance regime,  $|\dot{x}| \leq |\dot{x}_b|$ , and is kept at a maximum value outside this regime. All parameters and constants intruded here can be found in Ref. [49].

## References

- [1] A. Babarit, M. Guglielmi, A.H. Clément, Declutching control of a wave energy converter, *Ocean. Eng.* 36 (2009) 1015–1024.
- [2] J. Lucas, M. Livingstone, N. Vuorinen, J. Cruz, Development of a wave energy converter (WEC) design tool - application to the waveroller wec including validation of numerical estimates, in: Fourth International Conference on Ocean Energy, Dublin, Ireland, 2012.
- [3] R. Gomes, M. Lopes, J. Henriques, L. Gato, A. Falcão, The dynamics and power extraction of bottom-hinged plate wave energy converters in regular and irregular waves, *Ocean. Eng.* 96 (2015) 86–99.
- [4] P. Schmitt, H. Asmuth, B. Elsäßer, Optimising power take-off of an oscillating wave surge converter using high fidelity numerical simulations, *Int. J. Mar. Energy* 16 (2016) 196–208.
- [5] A. Babarit, J. Hals, M. Muliawan, A. Kurniawan, T. Moan, J. Krokstad, Numerical benchmarking study of a selection of wave energy converters, *Renew. Energy* 41 (2012) 44–63.
- [6] G.R. Liu, M.B. Liu, Smoothed Particle Hydrodynamics, World Scientific, 2003.
- [7] Y. Wei, A. Rafiee, A. Henry, F. Dias, Wave interaction with an oscillating wave surge converter. Part I: viscous effects, *Ocean. Eng.* 104 (2015) 185–203.
- [8] Y. Wei, T. Abadie, A. Henry, F. Dias, Wave interaction with an oscillating wave surge converter. Part II: Slamming, *Ocean. Eng.* 113 (2016) 319–334.
- [9] Y. Wei, T. Abadie, F. Dias, A cost-effective method for modelling wave-OWSC interaction, *Int. J. Offshore Polar Eng.* 27 (2017) 366–373.
- [10] P. Schmitt, B. Elsaesser, On the use of OpenFOAM to model oscillating wave surge converters, *Ocean. Eng.* 108 (2015) 98–104.
- [11] P.J. Martínez-Ferrer, L. Qian, D.M. Causon, C.G. Mingham, Z. Ma, Numerical simulation of wave slamming on a flap-type oscillating wave energy device, *Int. J. Offshore Polar Eng.* 28 (2018) 65–71.
- [12] S. Yeylaghi, B. Moa, P. Oshkai, B. Buckingham, C. Crawford, ISPH modelling of an oscillating wave surge converter using an OpenMP-based parallel approach, *J. Ocean Eng. Mar. Energy* 2 (2016) 301–312.
- [13] A.A. Shabana, Dynamics of Multibody Systems, Cambridge University Press, 2005.
- [14] H. Mazhar, T. Heyn, A. Pazouki, D. Melanz, A. Seidl, A. Bartholomew, A. Tasora, D. Negruț, CHRONO: a parallel multi-physics library for rigid-body, flexible-body, and fluid dynamics, *Mech. Sci.* 4 (2013) 49–64.
- [15] A. Tasora, R. Serban, H. Mazhar, A. Pazouki, D. Melanz, J. Fleischmann, M. Taylor, H. Sugiyama, D. Negruț, Chrono: an open source multi-physics dynamics engine, in: Lecture Notes in Computer Science, Springer International Publishing, 2016, pp. 19–49.
- [16] M. Gómez-Gesteira, B.D. Rogers, R.A. Dalrymple, A.J. Crespo, State-of-the-art of classical SPH for free-surface flows, *J. Hydraul. Res.* 48 (2010) 6–27.
- [17] J. Monaghan, Smoothed particle hydrodynamics and its diverse applications, *Annu. Rev. Fluid Mech.* 44 (2012) 323–346.
- [18] R.B. Canelas, A.J. Crespo, J.M. Domínguez, R.M. Ferreira, M. Gómez-Gesteira, SPH-DCDEM model for arbitrary geometries in free surface solid–fluid flows, *Comput. Phys. Commun.* 202 (2016) 131–140.
- [19] T. Verbrugghe, J.M. Domínguez, A.J. Crespo, C. Altomare, V. Stratigaki, P. Troch, A. Kortenhaus, Coupling methodology for smoothed particle hydrodynamics modelling of non-linear wave-structure interactions, *Coast Eng.* 138 (2018) 184–198.
- [20] M. Brito, O. García-Feal, J.M. Domínguez, A.J.C. Crespo, R.B. Canelas, R.M.L. Ferreira, M.G. Neves, Coupling between Dualsphysics and Chrono-Engine: towards large scale HPC multiphysics simulations, in: 11th SPHERIC International Workshop, Munich, Germany, 2016.
- [21] M. Brito, R.B. Canelas, R.M.L. Ferreira, O.G. Feal, J.M. Domínguez, C.C. A. J. L. Teixeira, M.G. Neves, Application, modelling and validation of an owsc using dualsphysics, in: 12th International SPHERIC Workshop 2017, 2017.
- [22] F. Dias, E. Renzi, S. Gallagher, D. Sarkar, Y. Wei, T. Abadie, C. Cummins, A. Rafiee, Analytical and computational modelling for wave energy systems: the example of oscillating wave surge converters, *Acta Mech. Sin.* 33 (2017) 647–662.
- [23] D. Zhang, Y. Shi, C. Huang, Y. Si, B. Huang, W. Li, SPH method with applications of oscillating wave surge converter, *Ocean. Eng.* 152 (2018) 273–285.
- [24] J. Monaghan, Simulating free surface flows with SPH, *J. Comput. Phys.* 110 (1994) 399–406.
- [25] A. Colagrossi, M. Landrini, Numerical simulation of interfacial flows by smoothed particle hydrodynamics, *J. Comput. Phys.* 191 (2003) 448–475.
- [26] A.J.C. Crespo, M. Gómez-Gesteira, R.A. Dalrymple, Boundary conditions generated by dynamic particles in SPH methods, *Comput. Mater. Continua (CMC)* 5 (2007) 173–184.
- [27] R. Canelas, M. Brito, O. Feal, J. Domínguez, A. Crespo, Extending DualSPHysics with a differential variational inequality: modeling fluid-mechanism interaction, *Appl. Ocean Res.* 76 (2018) 88–97.
- [28] A. Tasora, M. Anitescu, A matrix-free cone complementarity approach for

- solving large-scale, nonsmooth, rigid body dynamics, *Comput. Methods Appl. Mech. Eng.* 200 (2011) 439–453.
- [29] A. Crespo, J. Domínguez, B. Rogers, M. Gómez-Gesteira, S. Longshaw, R. Canelas, R. Vacondio, A. Barreiro, O. García-Feal, DualSPHysics: open-source parallel CFD solver based on smoothed particle hydrodynamics (SPH), *Comput. Phys. Commun.* 187 (2015) 204–216.
- [30] J.M. Domínguez, A.J. Crespo, M. Gómez-Gesteira, Optimization strategies for CPU and GPU implementations of a smoothed particle hydrodynamics method, *Comput. Phys. Commun.* 184 (2013) 617–627.
- [31] R.A. Gingold, J.J. Monaghan, Smoothed particle hydrodynamics: theory and application to non-spherical stars, *Mon. Not. R. Astron. Soc.* 181 (1977) 375–389.
- [32] L.B. Lucy, A numerical approach to the testing of the fission hypothesis, *Astron. J.* 82 (1977) 1013.
- [33] J.J. Monaghan, Smoothed particle hydrodynamics, *Annu. Rev. Astron. Astrophys.* 30 (1992) 543–574.
- [34] S. Marrone, M. Antuono, A. Colagrossi, G. Colicchio, D.L. Touzé, G. Graziani,  $\delta$ -SPH model for simulating violent impact flows, *Comput. Methods Appl. Mech. Eng.* 200 (2011) 1526–1542.
- [35] H. Wendland, Piecewise polynomial, positive definite and compactly supported radial functions of minimal degree, *Adv. Comput. Math.* 4 (1995) 389–396.
- [36] J.J. Monaghan, Smoothed particle hydrodynamics, *Rep. Prog. Phys.* 68 (2005) 1703–1759.
- [37] C. Altomare, J. Domínguez, A. Crespo, J. González-Cao, T. Suzuki, M. Gómez-Gesteira, P. Troch, Long-crested wave generation and absorption for SPH-based DualSPHysics model, *Coast Eng.* 127 (2017) 37–54.
- [38] R.B. Canelas, J.M. Domínguez, A.J. Crespo, M. Gómez-Gesteira, R.M. Ferreira, A smooth particle hydrodynamics discretization for the modelling of free surface flows and rigid body dynamics, *Int. J. Numer. Methods Fluids* 78 (2015) 581–593.
- [39] B.J. Leimkuhler, S. Reich, R.D. Skeel, Integration methods for molecular dynamics, in: J.P. Mesirow, K. Schulten, D.W. Sumners (Eds.), *Mathematical Approaches to Biomolecular Structure and Dynamics*, Springer, New York, 1996, pp. 161–185. New York, NY.
- [40] J.J. Monaghan, A. Kos, Solitary waves on a cretan beach, *J. Waterw. Port, Coast. Ocean Eng.* 125 (1999) 145–155.
- [41] J.J. Monaghan, A. Kos, N. Issa, Fluid motion generated by impact, *J. Waterw. Port, Coast. Ocean Eng.* 129 (2003) 250–259.
- [42] B. Bouscasse, A. Colagrossi, S. Marrone, M. Antuono, Nonlinear water wave interaction with floating bodies in SPH, *J. Fluids Struct.* 42 (2013) 112–129.
- [43] C. Altomare, A. Crespo, B. Rogers, J. Domínguez, X. Gironella, M. Gómez-Gesteira, Numerical modelling of armour block sea breakwater with smoothed particle hydrodynamics, *Comput. Struct.* 130 (2014) 34–45.
- [44] J.M. Domínguez, A.J.C. Crespo, J.L. Cercós-Pita, G. Fourtakas, B. Neves, Evaluation of reliability and efficiency of different boundary conditions in an SPH code, in: 10th SPHERIC International Workshop, Parma, Italy, 2015.
- [45] H. Mazhar, T. Heyn, D. Negruț, A. Tasora, Using nesterov's method to accelerate multibody dynamics with friction and contact, *ACM Trans. Graph.* 34 (32) (2015) 1–32, 14.
- [46] D.E. Stewart, Rigid-body dynamics with friction and impact, *SIAM Rev.* 42 (2000) 3–39.
- [47] M. Anitescu, G.D. Hart, A constraint-stabilized time-stepping approach for rigid multibody dynamics with joints, contact and friction, *Int. J. Numer. Methods Eng.* 60 (2004) 2335–2371.
- [48] M. Anitescu, Optimization-based simulation of nonsmooth rigid multibody dynamics, *Math. Program.* 105 (2006) 113–143.
- [49] M. Brito, L. Teixeira, R.B. Canelas, R.M.L. Ferreira, M.G. Neves, Experimental and numerical studies of dynamic behaviors of a hydraulic power take-off cylinder using spectral representation method, *J. Tribol.* 140 (2017b), 021102.
- [50] C. Altomare, A.J. Crespo, J.M. Domínguez, M. Gómez-Gesteira, T. Suzuki, T. Verwaest, Applicability of smoothed particle hydrodynamics for estimation of sea wave impact on coastal structures, *Coast Eng.* 96 (2015) 1–12.
- [51] A. Crespo, C. Altomare, J. Domínguez, J. González-Cao, M. Gómez-Gesteira, Towards simulating floating offshore oscillating water column converters with smoothed particle hydrodynamics, *Coast Eng.* 126 (2017) 11–26.
- [52] E. Mansard, E. Funke, The measurement of incident and reflected spectra using a least squares method, in: *Coastal Engineering*, American Society of Civil Engineers (ASCE), 1980.
- [53] Met-Flow, UVP Monitor User's Guide, 2002. Chemin Auguste-Pidou 8, 1007 Lausanne, Switzerland: Met-Flow S.A.
- [54] F.C. Ting, J.T. Kirby, Observation of undertow and turbulence in a laboratory surf zone, *Coast Eng.* 24 (1994) 51–80.
- [55] A.A. Dimas, K.A. Galani, Turbulent flow induced by regular and irregular waves above a steep rock-armored slope, *J. Waterw. Port, Coast. Ocean Eng.* 142 (2016), 04016004.
- [56] B.M. Count, D.V. Evans, The influence of projecting sidewalls on the hydrodynamic performance of wave-energy devices, *J. Fluid Mech.* 145 (1984) 361–376.
- [57] A.F. Falcão, Phase control through load control of oscillating-body wave energy converters with hydraulic PTO system, *Ocean. Eng.* 35 (2008) 358–366.
- [58] H. Yanada, Y. Sekikawa, Modeling of dynamic behaviors of friction, *Mechatronics* 18 (2008) 330–339.
- [59] X.B. Tran, N. Hafizah, H. Yanada, Modeling of dynamic friction behaviors of hydraulic cylinders, *Mechatronics* 22 (2012) 65–75.